J. Chem. Thermodynamics 145 (2020) 106069

Contents lists available at ScienceDirect

J. Chem. Thermodynamics

journal homepage: www.elsevier.com/locate/jct

Thermodynamic assessment of the KF-ThF_4, LiF-KF-ThF_4 and NaF-KF-ThF_4 systems

J.A. Ocádiz-Flores [a], E. Carré [b], J.-C. Griveau [c], E. Colineau [c], E. Capelli [a], P. Souček [c], O. Beneš [c], R.J.M. Konings [c], A.L. Smith [a,*]

[a] Delft University of Technology, Faculty of Applied Sciences, Radiation Science & Technology Department, Mekelweg 15, 2629 JB Delft, The Netherlands
[b] Chimie ParisTech-CNRS, Institut de Recherche de Chimie Paris 75005 Paris, France
[c] European Commission, Joint Research Centre, P.O. Box 2340, D-76125 Karlsruhe, Germany

ARTICLE INFO

Article history:
Received 26 April 2019
Received in revised form 13 January 2020
Accepted 25 January 2020
Available online 1 February 2020

Keywords:
CALPHAD
Molten Salt Reactor
Differential Scanning Calorimetry
X-ray diffraction
Thermal relaxation calorimetry

ABSTRACT

A thermodynamic assessment of the KF-ThF_4 binary system using the CALPHAD method is presented, where the liquid solution is described by the modified quasichemical formalism in the quadruplet approximation. The optimization of the phase diagram is based on experimental data reported in the literature and newly measured X-ray diffraction and differential scanning calorimetry data, which have allowed to solve discrepancies between past assessments. The low temperature heat capacity of α-K_2ThF_6 has also been measured using thermal relaxation calorimetry; from these data the heat capacity and standard entropy values have been derived at 298.15 K: $C^{o}_{p,m}(K_2ThF_6, \ cr, 298.15K) = (193.2 \pm 3.9)$ $J{\cdot}K^{-1} \cdot mol^{-1}$ and $S^{o}_{m}(K_2ThF_6, cr, 298.15K) = (256.9 \pm 4.8)$ $J{\cdot}K^{-1} \cdot mol^{-1}$. Taking existing assessments of the relevant binaries, the new optimization is extrapolated to the ternary systems LiF-KF-ThF_4 and NaF-KF-ThF_4 using an asymmetric Kohler/Toop formalism. The standard enthalpy of formation and standard entropy of $KNaThF_6$ are re-calculated from published e.m.f data, and included in the assessment of the ternary system. A calculated projection of the NaF-KF-ThF_4 system at 300 K and the optimized liquidus projections of both systems are compared to published phase equilibrium data at room temperature and along the LiF-$LiThF_5$ and NaF-$KThF_5$ pseudobinaries, with good agreement.

1. Introduction

The Generation IV International Forum, a group of fourteen member countries pursuing research and development for the next generation of nuclear reactors, has selected six nuclear energy systems [1,2]. Among these, the Molten Salt Reactor (MSR) is, in terms of safety and performance, one of the most promising nuclear reactor designs presently being studied. Its central characteristic is that the nuclear fuel is made of a molten fluoride (or chloride) salt instead of being a solid oxide or a metal. This liquid serves both as the fuel and coolant for the reactor. Two experimental MSRs have been built in the past: the Aircraft Reactor Experiment (ARE) [3] in 1954, and the Molten Salt Reactor Experiment (MSRE), which operated successfully between 1965-1969 [4]. A comprehensive knowledge of the physico-chemical properties of the salt is needed for the safety assessment and design of modern reactors, as the irradiated salt constitutes a complex and multi-component system.

The ^{7}LiF-NaF-KF-ThF_4-UF_4-AnF_3 (An= actinide) system has been proposed for the fuel of an actinide burner design [5], and still needs a full thermodynamic characterization. In particular, studies on many of the KF-containing systems are either absent in the literature or need to be revisited, namely KF-UF_3 (some intermediate compounds have been synthesized [6]), KF-UF_4 (phase diagram information exists [7], but a CALPHAD model is missing), KF-PuF_3 (there is no phase diagram information available), and KF-ThF_4. Two sets of authors, Emelyanov and Evstyukhin [8] and Asker et al. [9] have studied the potassium fluoride-thorium fluoride binary system, with fair agreement in some regions of the system. However, they have reported conflicting interpretations in other regions, which need to be resolved. To this end, we present a re-evaluation of the KF-ThF_4 binary system, using X-ray diffraction (XRD), Differential Scanning Calorimetry (DSC), and low temperature heat capacity measurements. A thermodynamic assessment using the CALPHAD method is moreover reported for the first time, where the Gibbs energy of the liquid solution is described using the quasi-chemical model in the quadruplet approximation. The assessment of the binary system is subsequently used to extrapolate to the ternary LiF-KF-ThF_4 and NaF-KF-ThF_4 systems.

---

* Corresponding author.
E-mail address: a.l.smith@tudelft.nl (A.L. Smith).

https://doi.org/10.1016/j.jct.2020.106069
0021-9614/

Table 1
Provenance and purity of the samples used in this study.

Formula	Source	State	Color	Mass fraction purity*	Purity analysis method
LiF	Alfa Aesar	Powder	White	0.9999 ± 0.0001	Provided by supplier
KF	Alfa Aesar	Powder	White	0.9999 ± 0.0001	Provided by supplier
NaF	Alfa Aesar	Powder	White	0.9999 ± 0.0001	Provided by supplier
ThF_4	JRC-Karlsruhe	Powder	White	0.995 ± 0.005	ICP-MS, XRD, DSC
K_2ThF_6	Solid-state synthesis	Powder	White	0.99 ± 0.01	XRD, DSC

[a]The secondary phase was K_2ThF_6.
* The quoted uncertainties correspond to standard uncertainties.

Table 2
Synthesis conditions.

Composition	Starting reagents[a]	High-temperature instrument[b]	Conditions[c]
$K_5ThF_9 + K_2ThF_6$	$(KF:ThF_4) = (0.833:0.167)$	Furnace	923 Kfor 12 h
$K_5ThF_9 + K_2ThF_6$	$(KF:ThF_4) = (0.750:0.250)$	Furnace	1073 K for 12 h
K_2ThF_6	$(KF:ThF_4) = (0.667:0.333)$	Furnace	873 K for 12 h
$K_2ThF_6 + K_7Th_6F_{31}$	$(KF:ThF_4) = (0.582:0.418)$	DSC	Max T = 1373 K, cooling 2 K/min
$KTh_2F_9 + KTh_6F_{25}$	$(KF:ThF_4) = (0.250:0.750)$	DSC	Max T = 1373 K, cooling 2 K/min
$KTh_2F_9 + KTh_6F_{25}$	$(KF:ThF_4) = (0.143:0.857)$	Furnace	1073 K for 12 h

[a] Standard uncertainty on the composition of the starting reagents was $u(X(ThF_4)) = 0.005$.
[b] The DSC measurements were performed at a pressure P = (0.10 ± 0.01) MPa. The syntheses in the furnace were carried out at a pressure P = (0.10 ± 0.04) MPa in the furnace. The quoted uncertainties correspond to the standard uncertainties.
[c] Standard uncertainties u are u(T) = 15 K for the furnace and u(T) = 10 K for the DSC temperature.

Table 3
Comparison between measured and available data for enthalpies of fusion of different salts at their respective fusion temperatures and (0.10 ± 0.01)[a] MPa.

Salt	Measured[a] $\Delta_{fus}H(T_{fus,salt})/kJ\cdot mol^{-1}$	Reference[b] $\Delta_{fus}H(T_{fus,salt})/kJ\cdot mol^{-1}$
LiF	25.9 ± 2.1	27.087 [17]
NaF	33.9 ± 2.8	33.3 [17]
KF	27.8 ± 2.3	27.2 [17]
ThF_4	38.7 ± 3.2	41.9 ± 2.0 [16]

[a] The quoted uncertainty corresponds to the standard uncertainty.
[b] Standard uncertainty not reported when not found in the reference.

2. Experimental methods

2.1. Sample preparation for DSC measurements

The purity of the four constituent salts, LiF (ultra-dry), NaF, KF, (all from Alfa Aesar, 0.9999 0.00010.9999 ± 0.0001[1] mass fraction purity) and ThF_4 was confirmed using X-ray diffraction (XRD) and Differential Scanning Calorimetry (DSC). NaF and KF had to be dried further, for 4 h at 673 K in an open nickel boat under Ar flow, in order to reach the adequate purity for thermodynamic measurements. ThF_4 was synthesized in JRC-Karlsruhe as described in [10]. All salts were of white color, and were handled in either powder or pressed pellet form. The experimental compositions reported hereafter were prepared by mixing either powder or pellet fragments of the pure salts in the corresponding stoichiometric ratios. As fluoride salts are highly sensitive to water and oxygen, handling and preparation of samples took place inside the dry atmosphere of an argon-filled glove box, where H_2O and O_2 content were kept below 1 ppm. (See Table 1)

2.2. Synthesis

The samples whose X-ray diffraction patterns are shown in this work were made by two methods. The first consisted in grinding powder mixtures and heating them inside a closed stainless steel crucible with a Ni liner in a tubular furnace under Ar flow. The second method consisted in heating powder mixtures in a DSC crucible above melting. The conditions are given below in Table 2.

2.3. Powder X-ray diffraction

X-ray powder diffraction (XRD) data were collected at room temperature (T = 293 ± 5 K[2]) using a PANalytical X'Pert PRO X-ray diffractometer and a Cu anode (0.4 mm x 12 mm line focus, 45 kV, 40 mA) by step scanning at a rate of 0.0104 $^{\circ}\cdot s^{-1}$ in the range $10^{\circ} < 2\theta < 120^{\circ}$ in a Bragg-Brentano configuration. The X-ray scattered intensities were measured with a real time multi strip (RTMS) detector (X'Celerator). Structural analysis was performed with the Rietveld and LeBail methods using the FullProf suite [11].

2.4. Differential Scanning Calorimetry

3D-heat flow DSC measurements were performed using a Setaram Multi-Detector HTC module of the 96 Line calorimeter under argon flow at a pressure of (0.10 ± 0.01 MPa[3]). All samples were placed inside a nickel liner and encapsulated for the calorimetric measurements inside a stainless steel crucible closed with a screwed bolt as described in [12] to avoid vaporization at high temperatures. Two kinds of information were sought using the DSC technique: phase diagram equilibria points and mixing enthalpies. In all cases the measurement program began with one heating cycle reaching 1483 K and was maintained at that temperature for at least 300 s to ensure complete mixing and melting of the end-members. In general, this first cycle was followed by three successive heating cycles with a heating rate ranging between 4 to 10 $K\cdot min^{-1}$, and 20–15-10–5 $K\cdot min^{-1}$ cooling rates. The procedure followed for the mixing enthalpy measurements is described in detail in Section 2.5.

Temperatures were monitored throughout the experiments by a series of interconnected S-type thermocouples. The temperature on the heating ramp was calibrated by measuring the melting points of standard high purity metals (In, Sn, Pb, Al, Ag, Au). The

---

[1] The reported uncertainty corresponds to the standard uncertainty.

[2] The reported uncertainty corresponds to the standard uncertainty.

[3] The reported uncertainty corresponds to the standard uncertainty.

Table 4
Thermodynamic data for end-members and intermediate compounds used in this work for the phase diagram assessment: $\Delta_f H^o_m(298\ K)/(kJ \cdot mol^{-1})$, $S^o_m(298\ K)/(J{\cdot}K^{-1} \cdot mol^{-1})$, and heat capacity coefficients $C_{p,m}(T/K)/(J{\cdot}K^{-1} \cdot mol^{-1})$, where $C_{p,m}(T/K) = a + b{\cdot}T + c{\cdot}T^2 + d{\cdot}T^{-2} + e{\cdot}T^3$. Optimized data are shown in bold.

Compound	$\Delta_f H^o_m(298\ K)/$ $(kJ{\cdot}mol^{-1})$	$S^o_m(298\ K)/$ $(J{\cdot}K^{-1} \cdot mol^{-1})$	$C_{p,m}(T/K)/(J{\cdot}K^{-1} \cdot mol^{-1}) = a + b{\cdot}T + c{\cdot}T^2 + d{\cdot}T^{-2} + e{\cdot}T^3$					Reference
			a	b	c	d	e	
LiF(cr)	−616.931	35.66	43.309	0.016312	$5.0470{\cdot}\ 10^{-7}$	$-5.691{\cdot}\ 10^{5}$		[14]
LiF(l)	−598.654	42.962	64.183					[14]
NaF(cr)	−576.650	51.21	47.63	0.01479		−464300		[14]
NaF(l)	−557.730	52.755	72.989					[14]
KF(cr)	−568.606	66.547	68.757414	$-5.775688{\cdot}10^{-2}$	$7.540486{\cdot}10^{-5}$	−766718.34	$-2.38856{\cdot}10^{-8}$	[14]
KF(l)	−554.374	67.769	71.965					[14]
ThF_4(cr)	−2097.900	142.05	122.173	0.00837		$-1.255{\cdot}10^{6}$		[15]
ThF_4(l)	−2103.654	101.237	170					[15,16]
Li_3ThF_7(cr)	−3960.259	236.1	282.100	0.05730	$1.514 \cdot 10^{-6}$	$-2.962{\cdot}10^{6}$		[24]
$LiThF_5$(cr)	−2719.490	181.89	165.482	0.02468	$5.047 \cdot 10^{-7}$	$-1.824{\cdot}10^{6}$		[24]
$LiTh_2F_9$(cr)	−4822.329	324.29	287.655	0.03305	$5.047 \cdot 10^{-7}$	$-3.079{\cdot}10^{6}$		[24]
$LiTh_4F_{17}$(cr)	−9021.140	609.0	532.001	0.04979	$5.047 \cdot 10^{-7}$	$-5.589{\cdot}10^{6}$		[24]
Na_4ThF_8(cr)	−4355.195	450.4	312.693	0.067530		$-3.11220{\cdot}10^{6}$		[26]
$Na_7Th_2F_{15}$(cr)	−8285.600	677.6	577.756	0.12027		$-5.76010{\cdot}10^{6}$		[26]
Na_2ThF_6(cr)	−3282.870	255.9	217.433	0.037950		$-2.18360{\cdot}10^{6}$		[26]
$Na_3Th_2F_{11}$(cr)	−5910.275	526.4	387.236	0.061110		−3902900		[26]
$Na_7Th_6F_{31}$(cr)	−16653.219	1364.0	1066.448	0.15375		$-1.07801{\cdot}10^{7}$		[26]
$NaThF_5$(cr)	−2693.871	199.2	169.803	0.023160		$-1.71930{\cdot}10^{6}$		[26]
$NaTh_2F_9$(cr)	−4791.776	348.3	291.976	0.031530		$-2.97430{\cdot}10^{6}$		[26]
K_5ThF_9-α(cr)	**−5048.000**	**473.0**	465.960	−0.28041	$3.77024{\cdot}10^{-4}$	$-5.088592{\cdot}10^{6}$	$-1.19428{\cdot}10^{-7}$	This work
K_5ThF_9-β(cr)	−5038.700	483.0	465.960	−0.28041	$3.77024{\cdot}10^{-4}$	$-5.088592{\cdot}10^{6}$	$-1.19428{\cdot}10^{-7}$	This work
K_2ThF_6-α(cr)	**−3340.000**	256.9	**208.616**	**0.03925**	**3.04459**$\cdot10^{-6}$	−**2.434407**$\cdot10^{6}$		This work
K_2ThF_6-β(cr)	−3318.000	280.0	**208.616**	**0.03925**	**3.04459**$\cdot10^{-6}$	−**2.434407**$\cdot10^{6}$		This work
K_3ThF_7(cr)	**−3837.250**	**411.5**	328.445	−0.16490	$2.26214{\cdot}10^{-4}$	$-3.555155{\cdot}10^{6}$	$-7.16569{\cdot}10^{-8}$	This work
K$_7$Th$_6$F$_{31}$(cr)	**−16938.800**	**1327.0**	1214.340	−0.35408	$5.27834{\cdot}10^{-4}$	$-1.2897028{\cdot}10^{7}$	$-1.67199{\cdot}10^{-7}$	This work
KTh_2F_9(cr)	**−4830.425**	**346.0**	313.103	−0.04102	$7.54049{\cdot}10^{-5}$	$-3.276718{\cdot}10^{6}$	$-2.38856{\cdot}10^{-8}$	This work
KTh$_6$F$_{25}$(cr)	**−13223.100**	**913.9**	801.795	$-7.53688{\cdot}\ 10^{-3}$	$7.54049{\cdot}10^{-5}$	$-8.296718{\cdot}10^{6}$	$-2.38856{\cdot}10^{-8}$	This work
$KNaThF_6$-α(cr)	**−3322.100**	**252.2**	238.560	−0.03460	$7.54049 \cdot 10^{-5}$	$-2.486018{\cdot}10^{6}$	$-2.38857{\cdot}10^{-8}$	This work, from [25]
$KNaThF_6$-β(cr)	−3306.800	270.7	238.560	−0.03460	$7.54049 \cdot 10^{-5}$	$-2.486018{\cdot}10^{6}$	$-2.38857{\cdot}10^{-8}$	This work, from [25]

temperature on the cooling ramp was obtained by extrapolation to 0 K·min^{-1} cooling rate. The melting temperatures of pure compounds and transition temperatures of mixtures were derived on the heating ramp as the onset temperature using tangential analysis of the recorded heat flow, while the liquidus temperatures of mixtures were taken as the minimum of the last thermal event as recommended in [13]. The data measured on the cooling ramp were not retained for the phase diagram optimization due to the occurrence of supercooling effects. The uncertainty on the measured temperatures is estimated to be ± 5 K for the pure compounds and ± 10 K for mixtures[4].

The DSC measurements support the purity indicated by the suppliers and XRD data, as the heat flow signal for each of the four salts (LiF, NaF, KF, ThF_4) showed only one peak corresponding to the melting event, and no peaks that could be assigned to impurities. The measured onset temperatures are in good agreement with the literature: (1118 ± 5 K), (1268 ± 5 K), (1129 ± 5 K), and (1381 ± 5 K[5]), respectively, vs. 1121.3 K (LiF, [14]), 1269.0 K (NaF, [14]), 1131.0 K (KF, [14]), and 1383.0 K (ThF_4, [15]).

2.5. Enthalpy of mixing measurements

Enthalpies of mixing measurements were made in the same DSC calorimeter as the aforementioned equilibrium data, using a technique described in detail in [16]. The starting end-members KF and ThF_4 materials were pressed into pellets. The KF pellet (compound with the lowest melting point) was placed under the ThF_4 pellet, with a Ni liner separating them to avoid eutectic melting upon heating. Upon melting of KF, the Ni liner sank to the bottom and solid ThF_4 came into contact with molten KF, and melted too. The enthalpy of mixing is then calculated as the difference between the measured heat and the melting enthalpies of the end-members:

$$\Delta_{mix}H^o(T_{fus,KF}) = \Delta_{meas}H^o(T_{fus,KF}) - x_{(1-ThF_4)}\Delta_{fus}H^o(KF, T_{fus,KF}) - x_{ThF_4}\Delta_{fus}H^o(ThF_4, T_{fus,KF}) \tag{1}$$

The values used for the enthalpies of fusion of KF and ThF_4 were taken from the SGTE database [17] and the work by Capelli et al. [16], respectively: Δ_{fus}H(KF) = 27.2 kJ·mol^{-1} and Δ_{fus}H(ThF_4) = (41.9 ± 2.0) kJ·mol^{-1}. As in the work by Capelli et al., the main assumption used in this method for ThF_4 is that the enthalpy of fusion is invariant with temperature, at least down to the melting point of the lower-melting salt, KF (T_{fus} = 1131 K). This assumption is supported by the fact that supercooling of ThF_4 is observed until 1081 K during cooling at 10 K/min, while the area of the peak is almost as large as for the 10 K/min heating curve which resulted in a melting event at the expected temperature of fusion (1381 ± 5) K[6].

The sensitivity of the calorimeter, from which the measured enthalpies are calculated, was determined on each individual

---

[4] The reported uncertainty corresponds to the standard uncertainty.

[5] The reported uncertainties for LiF, NaF, KF, and ThF_4 correspond to the standard uncertainty.

[6] The quoted uncertainty corresponds to the standard uncertainty.

run by using a silver standard in the reference crucible, as described in [16]. The sensitivity coefficient used to determine the mixing enthalpies was validated by testing on the end-members. The enthalpy of fusion of ThF_4 was measured to be: (38.7 ± 3.2)[7] $kJ{\cdot}mol^{-1}$, while that of KF was measured as (27.8 ± 2.3)[8] $kJ{\cdot}mol^{-1}$. Thus both measurements were within the stated uncertainties in agreement with the published values. Moreover, enthalpy of fusion measurements for LiF and NaF also gave values in agreement with the literature. The results are listed in Table 3 along with those of KF and ThF_4. These results give us good confidence in the chosen calibration factor. The errors reported in Table 7 are based on the propagation of the standard uncertainty of the sensitivity coefficient obtained from the calibration process.

2.6. Low temperature heat capacity

Low temperature heat capacity measurements were performed on m=7.29 mg[9] of K_2ThF_6 in the temperature range T= (1.8-298.5) K using a PPMS (Physical Property Measurement System, Quantum Design) instrument with no applied magnetic field. A critical assessment of this thermal relaxation calorimetry method can be found in [18]. The contributions of the sample platform, wires, and grease were taken into account by a separate measurement of an addenda curve. From previous studies with standard materials and other compounds [19,20], the relative standard uncertainty was estimated at about 2 % above 270 K, 1% from 100 to 270 K, and reaching about 3 % at the lowest temperatures [18,19].

3. Thermodynamic modelling

Optimizations of the phase diagrams were carried out by the CALPHAD (CALculation of PHase Diagram) method [21] using the Factsage software [22]. To carry out such an optimization, the identity of the phases present in the system of interest must be known, as well as their respective Gibbs energy functions.

3.1. Pure compounds

The Gibbs energy function of a pure compound is given by:

$$G(T) = \Delta_f H^{\circ}_{\mathrm{m}}(298) - S^{\circ}_{\mathrm{m}}(298)T + \int_{298}^{T} C_{\mathrm{p,m}}(T)dT - T\int_{298}^{T} \frac{C_{\mathrm{p,m}}(T)}{T}dT \tag{2}$$

where $\Delta_f H^{\circ}_{\mathrm{m}}(298)$ is the standard enthalpy of formation, $S^{\circ}_{\mathrm{m}}(298)$ is the standard absolute entropy, both evaluated at a reference temperature, in this case 298.15 K (throughout this work 298 will be understood to mean 298.15 K for simplicity), and $C_{\mathrm{p,m}}$ is the isobaric heat capacity expressed as a polynomial:

$$C_{\mathrm{p,m}}(T) = a + bT + cT^2 + dT^{-2} + eT^3 \tag{3}$$

with more terms added if necessary.

In this work, the Neumann-Kopp rule [23] applied to KF and ThF_4 was used to estimate the heat capacities of intermediate compounds in the absence of experimental data. The only exceptions were α-K_2ThF_6(cr) and β-K_2ThF_6(cr), for which a fit was made. The fit included the low temperature heat capacity points measured herein in the 250-300 K range as well as high temperature points given by the Neumann-Kopp rule in the 500-1500 K range. Moreover, the temperature-independent term of the heat capacity, a, was optimized such that (C_p(K_2ThF_6,(cr),298.15 K) = 193.2 $J{\cdot}K^{-1}\cdot mol^{-1}$, the same value found by fitting of the low temperature heat capacity data of α-K_2ThF_6(cr) (see Section 5.3).

Table 5
Cation-cation coordination numbers of the liquid solution.

A	B	$Z^{A}_{AB/FF}$	$Z^{B}_{AB/FF}$
Li^+	Li^+	6	6
Na^+	Na^+	6	6
K^+	K^+	6	6
Th^{4+}	Th^{4+}	6	6
Li^+	K^+	6	6
Na^+	K^+	6	6
Li^+	Th^{4+}	2	6
Na^+	Th^{4+}	2	6
K^+	Th^{4+}	3	6

The thermodynamic data for all compounds in this study are listed in Table 4. The convention used throughout this paper is that the lower temperature phases are denoted with α; the opposite convention is used by [9,8] (respectively: Figs. A.1 and A.2). The data for both solid and liquid alkali fluorides (LiF, NaF, KF) and ThF_4 were taken from [14,24], respectively. All thermodynamic functions of the intermediate compounds in the LiF-ThF_4 and NaF-ThF_4 systems were derived by optimization in [24], while those for intermediate compounds in the KF-ThF_4 system were obtained in this work by optimization using phase equilibrium and mixing enthalpy data.

The transition temperature and enthalpy of transition of K_5ThF_9 $(\Delta_{tr}H^{o}_{m} = (9.3 \pm 0.8)$ $kJ{\cdot}mol^{-1}, T_{tr}$ = 926 ± 5) K, K_2ThF_6 $(\Delta_{tr}H^{o}_{m} = (22.0 \pm 2.0)$ $kJ{\cdot}mol^{-1}, T_{tr}$ = 952 ± 5) K, and $KNaThF_6$ $(\Delta_{tr}H^{o}_{m} = (15.3 \pm 0.6)$ $kJ{\cdot}mol^{-1}, T_{tr}$ = 825 ± 5) K were measured in this work by DSC using a similar procedure to the mixing enthalpies with a silver standard in the reference crucible. The experimentally determined values were implemented in the model without further optimization.

No quaternary fluorides have been reported in the LiF-KF-ThF_4 system, while $KNaThF_6$ (which displays a phase transition) is the only quaternary fluoride reported in the NaF-KF-ThF_4 system [8], and its thermodynamic properties were studied by Mukherjee and Dash by means of DSC and solid electrolyte galvanic cell [25]. Based on the former technique, the authors derived the heat capacity in the temperature range 300-870 K, while with the latter, they obtained the Gibbs energy of formation in the temperature range 773-849 K from which they derived standard enthalpy of formation and standard entropy values at 298 K. The heat capacity reported by them results in an extremely stable phase, such that unreasonably high excess parameters would have to be applied to the liquid NaF-KF-ThF_4 solution in order to stabilize it even at high temperatures. For this reason, this work approximated the heat capacity function of $KNaThF_6$ using the Neumann-Kopp rule applied to NaF, KF, and ThF_4. In addition, we have reassessed the enthalpy of formation and entropy at 298 K based on the experimental data of [25] and carefully selected auxiliary data (see Appendix for details). The final optimized standard enthalpy of formation and standard entropy yield a Gibbs energy which is only $\sim$1 % larger than the experimental value.

---

[7] The quoted uncertainty corresponds to the standard uncertainty.

[8] The quoted uncertainty corresponds to the standard uncertainty.

[9] Standard uncertainties u are $u(m)$ = 0.05 mg.

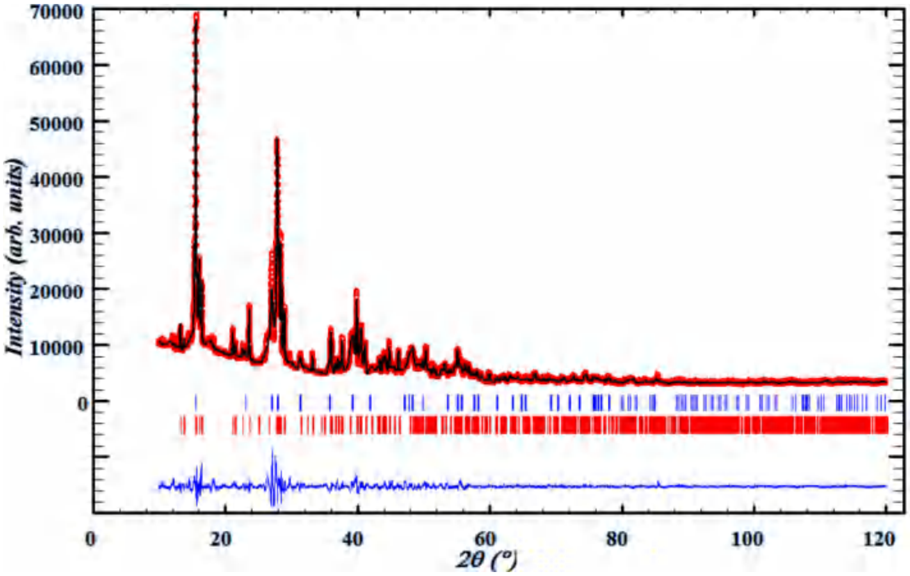

Fig. 1. Diffractogram of the K_5ThF_9-K_2ThF_6 mixture X(ThF_4) = 0.17. Comparison between the observed (Y_{obs}, in red) and calculated (Y_{calc}, in black) X-ray diffraction patterns. $Y_{obs} - Y_{calc}$, in blue, is the difference between the experimental and calculated intensities. The Bragg's reflection angular positions are marked in blue (K_2ThF_6), and red (K_5ThF_9). (For interpretation of the references to colour in this figure legend, the reader is referred to the web version of this article.)

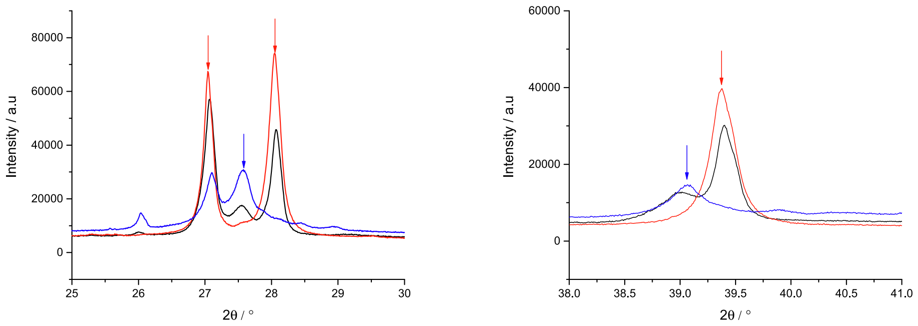

(a)

(b)

Fig. 2. Insets of the diffractogram of the sample of composition X(ThF_4) = 0.25, revealing Bragg reflections corresponding to the "K_3ThF_7" composition (black), compared to K_2ThF_6 (red) and K_5ThF_9 (blue). (For interpretation of the references to colour in this figure legend, the reader is referred to the web version of this article.)

3.2. Solid solution

The total Gibbs energy function of the two-component solid solutions in the present system is given by:

$$G(T) = X_1G^{o}_{m,1}(T) + X_2G^{o}_{m,1}(T) + X_1RTlnX_1 + X_2RTlnX_2 + G^{xs}_{m} \tag{4}$$

where X_i are the molar fractions and (T) $G^{o}_{m,i}$(T) are the standard molar Gibbs energies of the pure end members. The excess Gibbs energy parameter is described using the polynomial formalism:

$$G^{xs}_{m} = \sum_{i,j} X^{i}_{1}\cdot X^{j}_{2}\cdot L_{i,j} \tag{5}$$

where $L_{i,j}$ is a coefficient which may depend on temperature in the form of the general equation

$$L_{i,j} = A + BT + CTlnT + DT^2 \tag{6}$$

Solid solutions are formed in the NaF-KF and NaF-ThF_4 binary systems, with optimizations taken from the literature, shown in Eq. (7) [27] and (8) [28]:

$$G^{xs}_{(Na,K)F} = X_{NaF}X_{KF}\cdot 26750 + X^{3}_{NaF}X_{KF}\cdot 20000\,J\cdot mol^{-1} \tag{7}$$

$$G^{xs}_{(Na_x,Th_{1-x})F_{4-3x}} = X_{NaF}X^{2}_{ThF_4}\cdot(-15500) + X^{3}_{NaF}X_{ThF_4}\cdot 40000\,J\cdot mol^{-1} \tag{8}$$

3.3. Liquid solution

All excess Gibbs energy terms of liquid solutions presented here have been modelled using the modified quasi-chemical model proposed by Pelton et al. [29], in the quadruplet approximation. The quasi-chemical model is particularly well adapted to describe ionic liquids such as in the present system, as it allows to select the composition of maximum short-range ordering (SRO) by varying the ratio between the cation-cation coordination numbers $Z^{A}_{AB/FF}$ and $Z^{B}_{AB/FF}$ (the fluorine is in this case the only anion present). The quadruplet approximation assumes a quadruplet, composed of two anions and two cations, to be the basic unit in liquid solution, and the excess parameters to be optimized are those related to the following second-nearest neighbor (SNN) exchange reaction:

$$(A-F-A) + (B-F-B) \longrightarrow 2(A-F-B) \quad \Delta g_{AB/F} \tag{9}$$

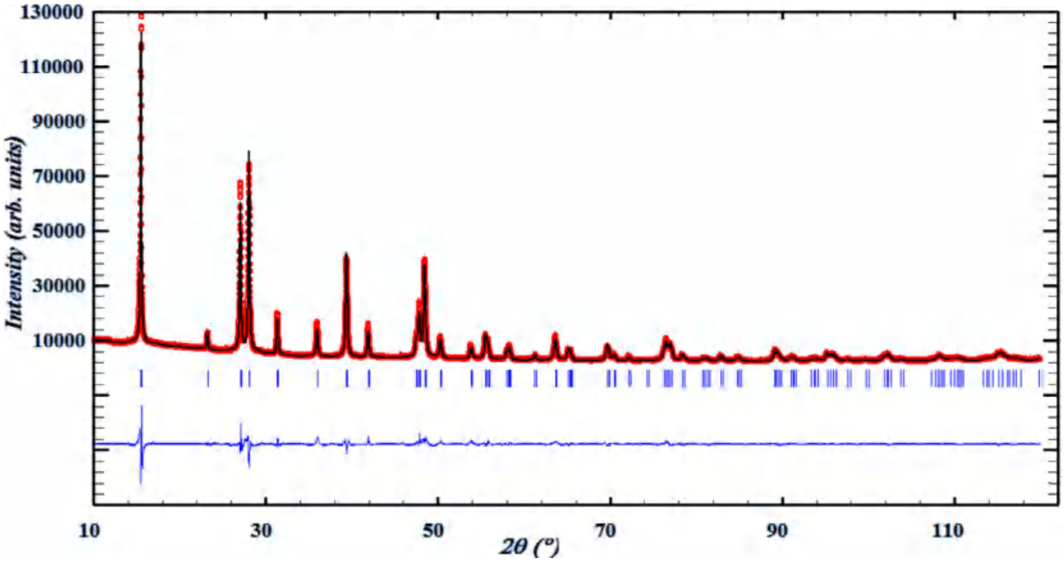

Fig. 3. XRD pattern of the pure hexagonal K_2ThF_6, X(ThF_4 = 0.33). Comparison between the observed (Y_{obs}, in red) and calculated (Y_{calc}, in black) X-ray diffraction patterns. $Y_{obs} - Y_{calc}$, in blue, is the difference between the experimental and calculated intensities. The Bragg's reflection angular positions are marked in blue. (For interpretation of the references to colour in this figure legend, the reader is referred to the web version of this article.)

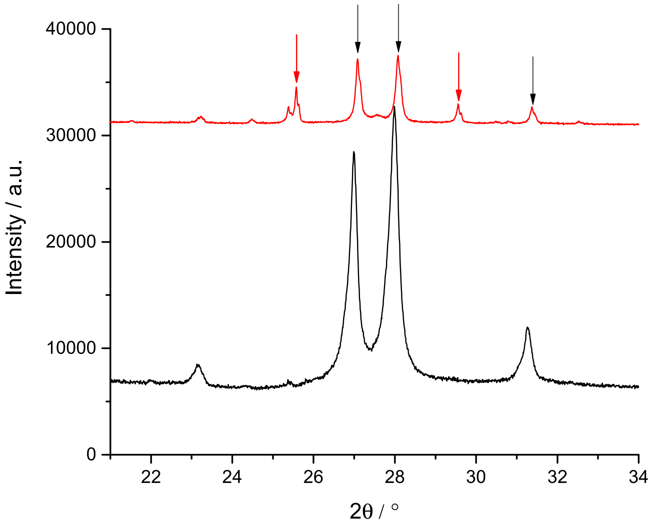

Fig. 4. Detail of the diffractogram of sample at composition X(ThF_4) = 0.33 after the first heating treatment at 973 K (red) and after a second annealing treatment at 873 K (black). The red arrows indicate Bragg reflections corresponding to the cubic phase, while the black arrows indicate those of the hexagonal phase. It is observed that the high temperature cubic phase disappears after the second annealing treatment, revealing a reversible phase transition. (For interpretation of the references to colour in this figure legend, the reader is referred to the web version of this article.)

where the fluoride anions are represented by *F*, and *A* and *B* denote the cations. $\Delta g_{AB/F}$ is the Gibbs energy change associated with the SNN exchange reaction, and has the following form:

$$\Delta g_{AB/F} = \Delta g^{o}_{AB/F} + \sum_{i\geqslant 1} g^{i0}_{AB/F}\chi^{i}_{AB/F} + \sum_{j\geqslant 1} g^{0j}_{AB/F}\chi^{j}_{BA/F} \qquad (10)$$

where $\Delta g^{o}_{AB/F}$ and $g^{ij}_{AB/F}$ are coefficients which may or may not be temperature-dependent, but which are independent of composition.

The dependence on composition is given by the $\chi_{AB/F}$ terms defined as:

$$\chi_{AB/F} = \frac{X_{AB}}{X_{AA} + X_{AB} + X_{BB}} \qquad (11)$$

where X_{AA}, X_{BB} and X_{AB} represent cation-cation pair mole fractions.

The anion coordination number is finally fixed by conservation of charge in the quadruplet:

$$\frac{q_A}{Z^{A}_{AB/FF}} + \frac{q_B}{Z^{B}_{AB/FF}} = \frac{2q_F}{Z^{F}_{AB/FF}} \qquad (12)$$

where q_i are the charges of the different ions, and $Z^{F}_{AB/FF}$ is the anion-anion coordination number, in this case fluorine-fluorine.

The cation-cation coordination numbers used in this work are listed in Table 5. These were chosen to represent the composition of maximum short-range ordering, where the Gibbs energy tends to have its minimum. In the case of KF-ThF_4, the point of maximum SRO can be reasonably expected to lie near X(ThF_4) = 0.33, i.e. where the liquid solution seems to be especially stable as indicated by the low liquidus in the vicinity of that composition. Hence, the cation-cation coordination numbers were chosen to fix maximum SRO around X(Th_4) = 0.33. Similarly, the cation-cation coordination numbers in the LiF-ThF_4 and NaF-ThF_4 systems were chosen to fix maximum SRO around X(Th_4) = 0.25, because the liquidus those phase diagrams is lowest in the vicinity of that composition.

The optimized excess Gibbs energy parameters of the binary liquid solution in the KF-ThF_4 system are shown in Eq. (13). The parameters were optimized based on the enthalpy of mixing data and on the phase diagram equilibria points of the liquidus. The excess Gibbs energy parameters of the other binary liquid solutions needed to calculate the ternary systems are given in Appendix F.

$$\Delta g_{KTh/FF} = -35472 + (-14644 + 8.35 \cdot T)\chi_{KTh/FF} + (-8786 + 9 \cdot T)\chi_{ThK/FF}\, J \cdot mol^{-1} \qquad (13)$$

3.4. Higher order systems

The ternary diagrams LiF-KF-ThF_4 and NaF-KF-ThF_4 have each been extrapolated from the constituting binary sub-systems using the asymmetric Toop formalism [30]. The salts belong to two groups of symmetry based on their tendency to remain as dissociated ionic liquids (LiF, NaF, KF) or to form molecular species in the melt (ThF_4). The optimized excess ternary parameters are:

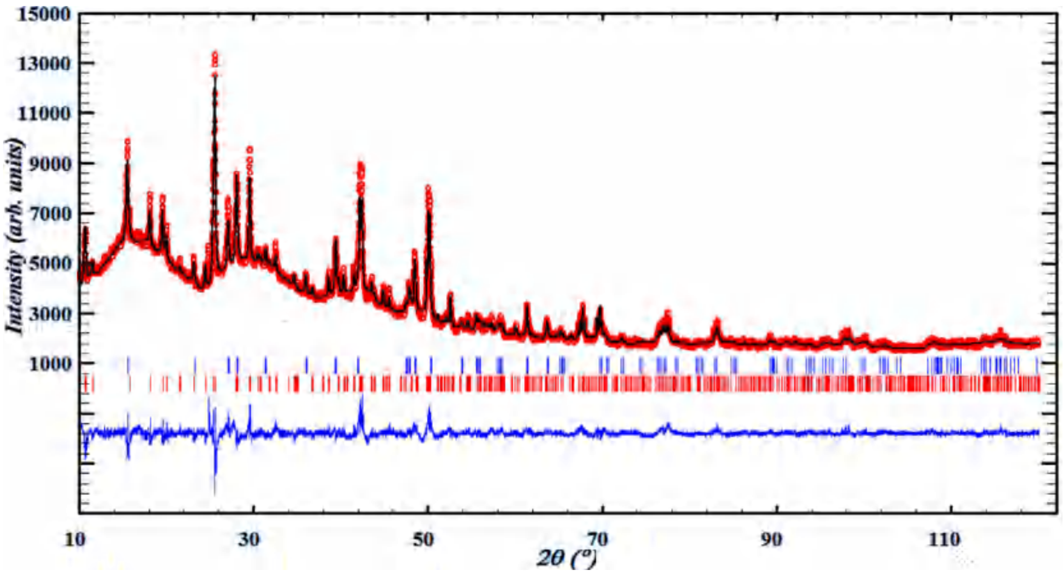

Fig. 5. XRD pattern of a sample with composition X(ThF_4) = 0.418 after DSC measurements. Comparison between the observed (Y_{obs}, in red) and calculated (Y_{calc}, in black) X-ray diffraction patterns. $Y_{obs} - Y_{calc}$, in blue, is the difference between the experimental and calculated intensities. The Bragg's reflection angular positions are marked in blue (K_2ThF_6), and red ($K_7Th_6F_{31}$). (For interpretation of the references to colour in this figure legend, the reader is referred to the web version of this article.)

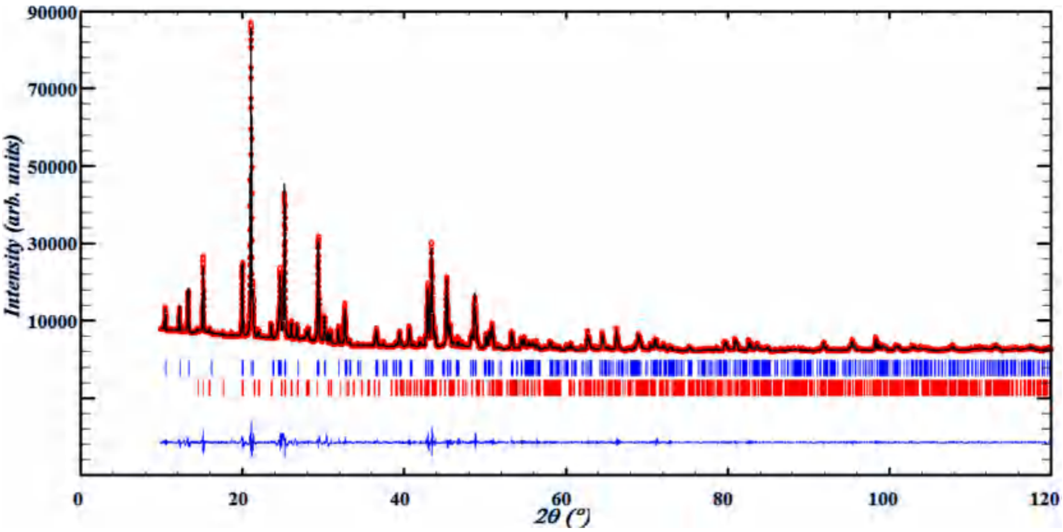

Fig. 6. XRD pattern of a sample with composition at X(ThF_4) = 0.857. Comparison between the observed (Y_{obs}, in red) and calculated (Y_{calc}, in black) X-ray diffraction patterns. $Y_{obs} - Y_{calc}$, in blue, is the difference between the experimental and calculated intensities. The Bragg's reflection angular positions are marked in blue (KTh_6F_{25}), and red (KTh_2F_9). (For interpretation of the references to colour in this figure legend, the reader is referred to the web version of this article.)

$$\Delta g_{ThLi(K)/FF} = 3000\,\mathrm{J \cdot mol^{-1}} \tag{14}$$

$$\Delta g_{KTh(Li)/FF} = 1000\,\mathrm{J \cdot mol^{-1}} \tag{15}$$

$$\Delta g_{LiK(Th)/FF} = 3000\,\mathrm{J \cdot mol^{-1}} \tag{16}$$

$$\Delta g_{KTh(Na)/FF} = -5000\,\mathrm{J \cdot mol^{-1}} \tag{17}$$

4. Previous evaluations of the KF-ThF_4 system

Phase diagram studies of this system have been reported by Bergman and Dergunov [31], Asker et al. [9] (Fig. A.1), and Emelyanov and Evstyukhin [8] (Fig. A.2). Bergman and Dergunov report a phase diagram which is certainly too simple, with four eutectics and three congruent melting points corresponding to the compounds K_3ThF_7, $KThF_5$, and KTh_3F_{13}; these results markedly differ from those of the other two authors. Emelyanov and Evstyukhin [8] and Asker et al. [9] agree on the existence of K_5ThF_9, K_3ThF_7, $KThF_5$, and K_2ThF_9, and the melting points they report for these compounds are similar. However, they report different ternary compounds for close compositions: KTh_3F_{13} (X(ThF_4) = 0.75, [9]) vs. KTh_6F_{25} (X(ThF_4) = 0.85, [8]); K_2ThF_6 (X(ThF_4) = 0.33, [9]) vs. $K_3Th_2F_{11}$ (X(ThF_4) = 0.4 [8]). Unlike the former pair, for which similar melting points were reported, K_2ThF_6 and $K_3Th_2F_{11}$ are reported to have dissimilar behavior: the former with a peritectic decomposition at 1023 K, and the latter with a congruent melting at 1160 K. In addition, these authors find different allotropic transformations: Asker et al. report two phases for K_5ThF_9 and K_2ThF_6, while Emelyanov and Evstyukhi report two phases only for KTh_2F_9. Finally, Asker et al. suggest the existence of a solid solution close to

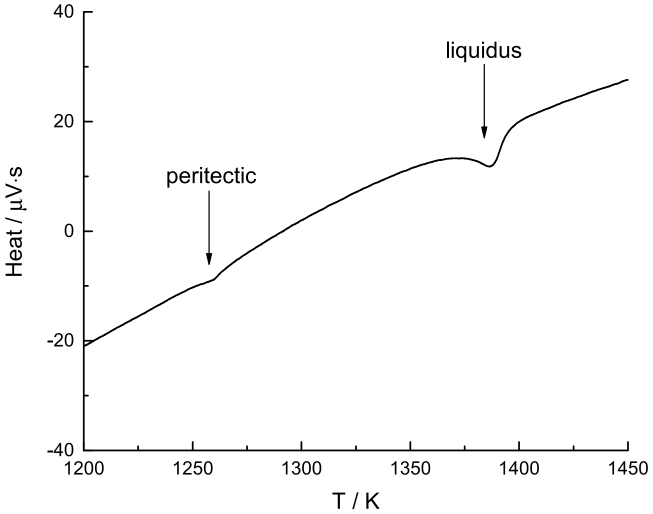

Fig. 7. Representative DSC signal of a sample with high ThF_4 content: X (ThF_4) = 0.979. There are two events which we assigned to a peritectic decomposition and liquidus.

pure ThF_4, yet Emelyanov and Evstyukhin do not. Our studies focused on exploring the differences found between the two sets of authors.

5. Results and discussion

5.1. Phase diagram studies in the KF-ThF_4 system

5.1.1. K_5ThF_9

Attempts to synthesize K_5ThF_9 did not yield pure K_5ThF_9, but a mixture with K_2ThF_6 (diffractogram shown in Fig. 1). K_5ThF_9 has orthorhombic symmetry space group $Cmc2_1$ [32]), with a diffractogram with many small reflections, while K_2ThF_6 is hexagonal (space group $P\bar{6}2$ m [33]). The structure could be refined with the model proposed by Ryan and Penneman [32], with distorted anti-prism for K and Th, and pentagonal bipyramid for the polyhedra of K. The refined cell parameters and table of atomic positions are reported in Appendix C.

Our DSC data from a sample made with a stoichiometric mixture of KF and ThF_4 powders suggest a first transition taking place at (926 ± 10) K, which is higher than the transition temperature recorded by Asker et al. (908 K), but similar to the temperature that Evstyukhin and Emelyanov attribute to the first eutectic of the system (935 K). We assign the event to an allotropic transition as the thermogram at this composition shows three other thermal events which are coherent with the existence of a high temperature K_5ThF_9 phase: eutectic, (968 ± 10 K), peritectic decomposition, (982 ± 10 K), and liquidus (1013 ± 10 K). With a measurement in the DSC using a silver reference method, the enthalpy of transition for K_5ThF_9 was found to be $\Delta_{tr}H^o_m = (9.3 \pm 0.8)$ kJ·mol^{-1}.

5.1.2. K_3ThF_7

K_3ThF_7 is not stable at room temperature according to Asker et al. [9] (Fig. A.2). The main goal of the present investigation at this composition was to confirm its eutectoid decomposition into K_2ThF_6 and K_5ThF_9 around 840 K as reported by [9]. The XRD pattern indeed revealed a mixture of K_2ThF_6 and K_5ThF_9, as illustrated in Figs. 2a and 2b. Although a satisfactory Rietveld refinement of the XRD pattern of the sample could not be obtained because of the poor crystallinity of the K_5ThF_9 phase in the mixture, the main Bragg reflections of both phases could clearly be identified, such that we were able to confirm that K_3ThF_7 is not stable at room temperature.

5.1.3. K_2ThF_6

K_2ThF_6 was successfully synthesized in pure form (hexagonal in space group $P\bar{6}2$ m [33], Fig. 3). A Rietveld refinement of the XRD data showed the sample was the low temperature hexagonal phase. In another attempt (Fig. 4), the synthesized sample was a mixture of the two phases reported in the literature, the high temperature phase being cubic and belonging to the space group $Pm\bar{3}m$ [33]. After a second annealing of this mixture at 873 K, below the transition temperature (918 K [9]), the diffractogram (Fig. 4) no longer showed any Bragg reflections attributable to the cubic phase, indicating the complete transformation of the cubic phase to the hexagonal form (Fig. 3). The DSC measurement of pure α-K_2ThF_6 shows an event at (952 ± 10) K which is higher than the temperature assigned by Asker et al. to the allotropic transformation (918 K). Using a silver reference the enthalpy of transition was measured to be kJ$\Delta_{tr}H^o_m = (22.0 \pm 2.0)$ kJ·mol^{-1}.

5.1.4. $K_7Th_6F_{31}$

Both previously reported phase diagrams and a study by Zachariasen during the Manhattan project agree on the existence of $KThF_5$ (rhombohedral in space group $R\bar{3}$, [33]). A compound with this composition has not been described in later structural works,

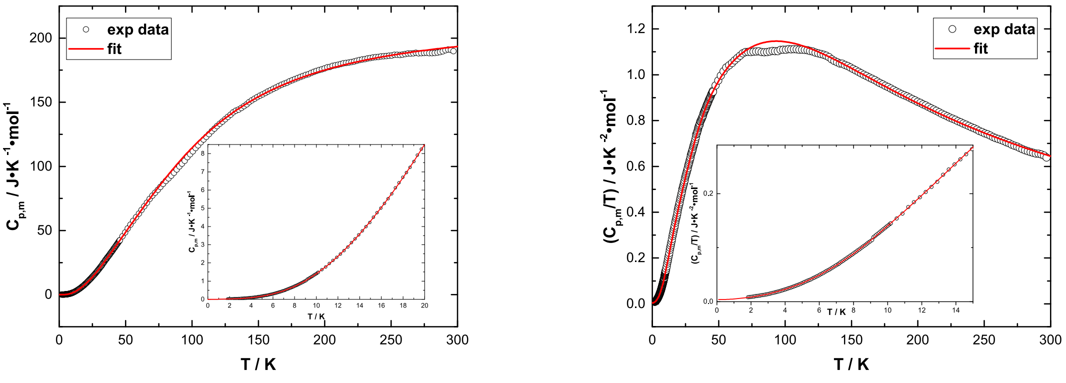

(a) $C_{p,m}$

(b) $C_{p,m}/T$

Fig. 8. Heat capacity of K_2ThF_6 (○) measured in zero magnetic field and fit to the data (red line): (a) $C_{p,m}$ and (b) $C_{p,m}$/T. (For interpretation of the references to colour in this figure legend, the reader is referred to the web version of this article.)

Table 6
Summary of fitting parameters of the heat capacity of K_2ThF_6 within the temperature range T = (1.8 to 10.0) K and T = (10.0 to 297.0) K.

Harmonic lattice-model		Debye and Einstein fit	
Temp. range/K	1.8–10.0	Temp. range/K	10.0–298.5
γ/mJ·mol^{-1} · K^{-2}	0.00389	n_D/mol	1.1135
B_3/mJ·mol^{-1} · K^{-4}	0.00111	θ_D/K	115.24
B_5/mJ·mol^{-1} · K^{-6}	$4.79569{\cdot}10^{-6}$	n_{E1}/mol	2.8066
B_7/mJ·mol^{-1} · K^{-8}	$-2.23822{\cdot}10^{-8}$	θ_{E1}/K	187.12
		n_{E2}/mol	4.5253
		θ_{E2}/K	392.70
		$n_D + n_{E1} + n_{E2}$/mol	8.4

Table 7
Mixing enthalpy of the $(1-x)$KF(l) + xThF$_4$(l) system determined in this work at T = 1131 ± 10 K and (0.10 ± 0.01)[d] MPa. KF melts at the measurement temperature, while ThF$_4$ is solid, although the initial state is taken to be a hypothetical liquid. The final state was an undercooled liquid mixture. The scanning temperature range was from (303 ± 10) K to (1373 ± 10) K.

X(ThF$_4$)[a]	$\Delta_{mix}H_m^o$ [b]/kJ·mol^{-1}	m(KF)/mg[c]	m(ThF$_4$)/mg[c]
0.109	−15.0 ± 1.4	29.2	18.9
0.200	−29.5 ± 1.8	23.6	31.3
0.305	−30.3 ± 0.2	21.9	50.9
0.338	−30.8 ± 1.0	14.9	40.4
0.401	−31.7 ± 0.7	57.9	16.3
0.504	−32.9 ± 3.0	39.3	7.3

[d] The quoted uncertainty corresponds to the standard uncertainty.
[a] Standard uncertainties u are u(X(ThF$_4$)) = 0.005.
[b] The error is based on the standard uncertainty determined during calibration.
[c] Standard uncertainties u are u(m) = 0.1 mg.

however. Rather, later studies identify $K_7Th_6F_{31}$ as the line compound in the neighborhood of X(ThF$_4$) = 0.5. This was first reported at Oak Ridge National Laboratory [34], where having studied other (AF:ThF$_4$)=(7:6) compounds in alkali fluoride-thorium tetrafluoride systems, the authors predicted the existence of such a compound in the KF-ThF$_4$ system and confirmed its existence with thermal analysis of slowly cooled melts. Indeed, a melt of composition X (ThF$_4$) = 0.462 displayed a single event upon slow cooling and a single phase according to post-characterization by XRD. By comparing the XRD data of this phase with the spacings for $Na_7U_6F_{31}$ and $K_7U_6F_{31}$, the authors were able to classify it as having rhombohedral symmetry. Moreover, the melting temperature, (1172 ± 2) K, was very close to that reported for KThF$_5$: 1178 K [9] and 1166 K [8]. Brunton [35] and more recently Grzechnik et al. [36] were able to fully solve the crystal structure of $K_7Th_6F_{31}$ ($R\bar{3}$), both using single-crystal X-ray diffraction data. A sample of composition X(ThF$_4$)= 0.418 (after having been subjected to a DSC measurement) was found in this work to be a mixture of K_2ThF_6 and $K_7Th_6F_{31}$ according to the Rietveld refinement (Fig. 5) of the XRD data. Supporting this result is a sample of mole fraction X(ThF$_4$)= 0.494 (between KF:ThF$_4$= 7:6 and 1:1 compositions) measured in the DSC which did not show thermal events close to 950 or 1000 K (corresponding to the equilibria of K_2ThF_6); these equilibria would be visible between K_2ThF_6 and the putative compound KThF$_5$ if $K_7Th_6F_{31}$ were not a stable phase (see Fig. 11). Finally, due to the lack of convincing experimental evidence for the existence of KThF$_5$, in particular the absence of reported Wyckoff positions, we discarded it from the phase diagram.

5.1.5. KTh_6F_{25}

To discern whether the phase with the highest thorium content was KTh_3F_{13} or KTh_6F_{25}, we attempted a synthesis of both compounds (see Table 2). The XRD pattern of the sample with composition X(ThF$_4$) = 0.857 was found to be a mixture of KTh_2F_9 (space group *Pnma*) and KTh_6F_{25} (space group $P6_3mmc$) from a LeBail refinement (Fig. 6). Unreacted excess KF was possibly not detected by XRD. In the same manner, the sample with composition X(ThF$_4$) = 0.75 revealed reflections corresponding to KTh_2F_9 and KTh_6F_{25}. Furthermore, KTh_3F_{13} is not mentioned in the literature outside the work of Asker et al., which brings further doubt on its existence. The phase was hence not retained in the present thermodynamic assessment.

5.2. Solid solution

Asker et al. [9] report the existence of a solid solution between KTh_3F_{13} and ThF$_4$ extending up to about 16 % KF in ThF$_4$. No evidence for such solid solution was found in the present DSC measurements, however, for three compositions between KTh_6F_{25} and ThF$_4$: X(ThF$_4$)= 0.902, 0.942, 0.979. These measurements only showed two thermal events (Fig. 7) which we assign to the peritectic decomposition of KTh_6F_{25} and liquidus.

5.3. Low temperature heat capacity of α-K_2ThF_6

The low temperature heat capacity data of α-K_2ThF_6 measured in the temperature range T=(1.8-298.5) K are shown in Fig. 8a

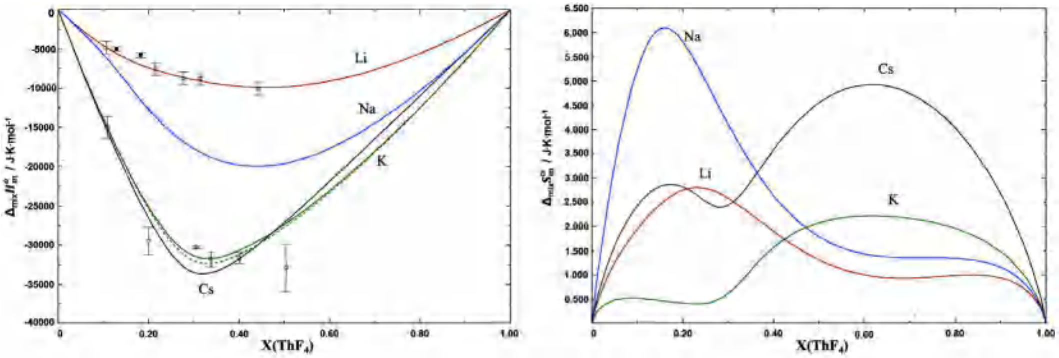

(a) Mixing enthalpies (b) Mixing entropies

Fig. 9. (a) Mixing enthalpies and (b) mixing entropies of the LiF-ThF$_4$ (red) [16], NaF-ThF$_4$ (blue) [24], KF-ThF$_4$ (green, this work) and CsF-ThF$_4$ (black) [42]. The calculations were done at T = 1400 K considering KF(l) and ThF$_4$(l) as initial states and the liquid solution as the final state.Circles: experimentally measured enthalpies of KF(l)-ThF$_4$(s) mixing at 1131 K (see Table 7); squares: experimentally measured points by [16] at 1121 K (LiF(l)-ThF$_4$(s), white) and 1383 K (LiF(l)-ThF$_4$(l), black).The dashed green line corresponds to KF-ThF$_4$ at T = 1131 K. Initial states were KF(l) and (hypothetical) ThF$_4$(l), the final state was the liquid solution (hypothetical for most of the composition range). (For interpretation of the references to colour in this figure legend, the reader is referred to the web version of this article.)

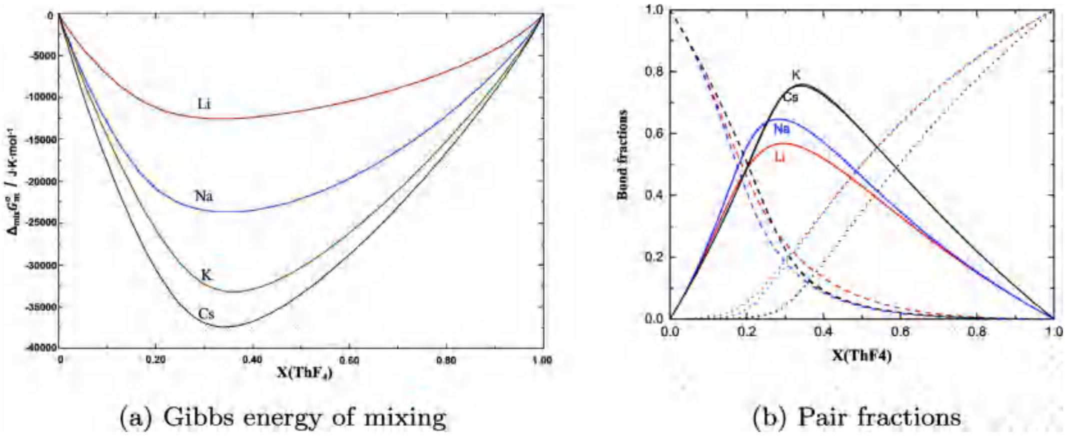

(a) Gibbs energy of mixing (b) Pair fractions

Fig. 10. (a) Gibbs energy of mixing at T = 1400 K. Red: LiF-ThF$_4$, blue: NaF-ThF$_4$, green: KF-ThF$_4$, black: CsF-ThF$_4$. Initial states were the liquid end-members, the final state was the liquid solution. (b) Bond fractions of the LiF-ThF$_4$ (red) [16], NaF-ThF$_4$ (blue) [24], KF-ThF$_4$ (green, this work) and CsF-ThF$_4$ (black) [42] systems calculated at T = 1400 K. Dashed lines: M-M-F-F, solid lines: M-Th-FF, dotted lines: Th-Th-F-F pair fractions. (For interpretation of the references to colour in this figure legend, the reader is referred to the web version of this article.)

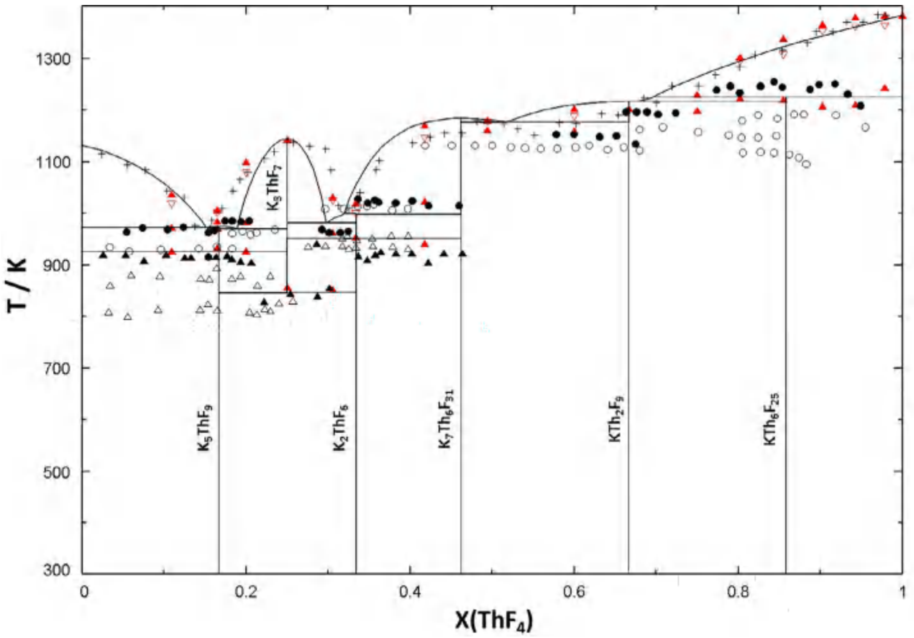

Fig. 11. Optimized KF-ThF$_4$ phase diagram superimposed against experimental points by Asker et al. (▲,+,●) [9], Emelyanov and Evstyukhin (△, ●) [8], and this study (▲, liquidus onset ▽, red). (For interpretation of the references to colour in this figure legend, the reader is referred to the web version of this article.)

and listed in Table A.3. The heat capacity reaches values that are about 40 J·K^{-1} · mol^{-1} below the classical Dulong-Petit limit ($C_{lat} = 3nR \sim 224$ J·K^{-1} · mol^{-1} for the nine atoms in the formula unit) as the temperature approaches 298.15 K. The collected data exhibit an anomaly in the neighborhood of the 65-120 K range, evident in the plot of C_p/T (Fig. 8b). Repeated operation of the instrument with diverse reference samples has shown that this is a systematic error attributable to the specific measuring puck upon which the sample is placed, and not an intrinsic feature of the measured material. This error is corrected by the fitted curve.

The thermodynamic functions of α-K$_2$ThF$_6$ were derived at 298.15 K by fitting the experimental data using the OriginPro 2015 software to theoretical functions below T= 10.0 K [37], and a combination of Debye and Einstein heat capacity functions [38–40] from T= (10.0 to 297.0) K. The fitting was done with the Levenbergh Marquardt iteration algorithm, using Origin C type fitting function above T= 10.0 K, and a simple harmonic lattice-type function below T= 10.0 K. The fitted data are shown with solid lines in Figs. 8a and 8b.

In the low temperature limit (T < 10.0 K), the phonon contribution can be adequately approximated by the harmonic lattice model [37], the form of which is given in Eq. 18:

$$C_{latt} = \sum B_n T^n, \quad where\ n = 3, 5, 7, 9 \ldots \tag{18}$$

Three terms, with coefficients listed in Table 6, were used over the temperature range T= (1.9 to 10.0) K. The electronic contribution of the conduction electrons at the Fermi surface are represented with a linear term γT [41]. In this case, K$_2$ThF$_6$ being a poor conductor, the electronic specific heat is nearly zero.

In the region 10.0 < T < 297.0 K the main contribution comes from the lattice term, modelled here with a combination of Debye

Table 8
Equilibrium data in the KF-ThF_4 system as measured in this work by DSC.

$X(ThF_4)$[a]	T/K[b]	Equilibrium	Equilibrium reaction
0.000	1129	KF congruent melting	KF = L
0.109	926	Polymorphic transition	K_5ThF_9-α = K_5ThF_9-β
0.109	971	Eutectic	KF + K_5ThF_9-β = L
0.109	1036	Liquidus	KF + L' = L
0.165	931	Polymorphic transition	K_5ThF_9-α = K_5ThF_9-β
0.165	968	Eutectic	KF + K_5ThF_9-β = L
0.165	982	Peritectic	K_5ThF_9-β = K_3ThF_7 + L
0.165	1005	Liquidus	K_3ThF_7 + L = L'
0.167	919	Polymorphic transition	K_5ThF_9-α = K_5ThF_9-β
0.167	966	Eutectic	KF + K_5ThF_9-β = L
0.167	1057	Liquidus	K_3ThF_7 + L = L'
0.200	925	Polymorphic transition	K_5ThF_9-α = K_5ThF_9-β
0.200	982	Peritectic	K_5ThF_9-β = K_3ThF_7 + L
0.200	1098	Liquidus	K_3ThF_7 + L' = L
0.25	856	Eutectoid	K_3ThF_7 = K_5ThF_9-α + K_2ThF_6-α
0.25	1141	Congruent melting	K_3ThF_7 = L
0.305	851	Eutectoid	K_3ThF_7 = K_5ThF_9-α + K_2ThF_6-α
0.305	961	Eutectic	K_3ThF_7 + K_2ThF_6-β = L
0.305	1029	Liquidus	K_3ThF_7 + L' = L
0.333	952	Polymorphic transition	K_2ThF_6-α = K_2ThF_6-β
0.333	1000	Peritectic	K_2ThF_6-β = $K_7Th_6F_{31}$ + L
0.418	940	Polymorphic transition	K_2ThF_6-α = K_2ThF_6-β
0.418	1021	Peritectic	K_2ThF_6-β = $K_7Th_6F_{31}$ + L
0.418	1169	Liquidus	$K_7Th_6F_{31}$ + L' = L
0.494	1159	Eutectic	$K_7Th_6F_{31}$ + K_2ThF_9 = L
0.494	1178	Liquidus	$K_7Th_6F_{31}$ + L' = L
0.600	1157	Eutectic	$K_7Th_6F_{31}$ + K_2ThF_9 = L
0.600	1201	Liquidus	K_2ThF_9 + L' = L
0.666	1202	Congruent Melting	K_2ThF_9 = L
0.749	1197	Eutectic	K_2ThF_9 + KTh_6F_{25} = L
0.749	1218	Peritectic	KTh_6F_{25} = L + ThF_4
0.802	1221	Peritectic	KTh_6F_{25} = L + ThF_4
0.802	1300	Liquidus	ThF_4 + L' = L
0.855	1218	Peritectic	KTh_6F_{25} = L + ThF_4
0.855	1336	Liquidus	ThF_4 + L' = L
0.902	1206	Peritectic	KTh_6F_{25} = L + ThF_4
0.902	1365	Liquidus	ThF_4 + L' = L
0.942	1209	Peritectic	KTh_6F_{25} = L + ThF_4
0.942	1379	Liquidus	ThF_4 + L' = L
0.979	1241	Peritectic	KTh_6F_{25} = L + ThF_4
0.979	1383	Liquidus	ThF_4 + L' = L
1.000	1381	Congruent melting	ThF_4 = L

[a] Standard uncertainties u are $u(X(ThF_4))$ = 0.005.
[b] Standard uncertainties u are u(T)= 5 K for the pure end-members, u(T) = 10 K for mixtures. The pressure was (0.10 ± 0.01) MPa.

and Einstein functions, denoted by $D(\theta_D)$ and $E(\theta_E)$, respectively, shown in Eq. (19):

$$C_{p,m} = n_D D(\theta_D) + n_{E1}E(\theta_{E1}) + n_{E2}E(\theta_{E2}) \tag{19}$$

Two Einstein functions were needed in order to achieve an adequate fit of the data, which was carried out excluding the problematic 65-120 K region. The fitted coefficients are listed in Table 6. The sum over n atoms is equal to 8.4, quite close to 9 as should be expected. The Debye and Einstein functions have the following forms:

$$D(\theta_D) = 9R\left(\frac{1}{x}\right)^3 \int_0^x \frac{exp(x)x^4}{[exp(x)-1]^2}\cdot dx, \quad x = \frac{\theta_D}{T} \tag{20}$$

$$E(\theta_E) = 3Rx^2 \frac{exp(x)}{[exp(x)-1]^2}, \quad x = \frac{\theta_E}{T} \tag{21}$$

where the universal gas constant is denoted by R and is equal to 8.3144598 $J{\cdot}K^{-1}\cdot mol^{-1}$.

The heat capacity value at 298.15 K obtained by interpolation is $C^o_{p,m}(K_2ThF_6, cr, 298.15\ K) = (193.2\pm\ 3.9)\ J{\cdot}K^{-1}\cdot mol^{-1}$. The experimental standard entropy at 298.15 K determined by numerical integration of $(C_{p,m}/T) = f(T)$ using the aforementioned fitted functions, is

$S^o_m(K_2ThF_6, cr, 298.15\ K) = (256.9\pm\ 4.8)$[10] $J{\cdot}K^{-1}\cdot mol^{-1}$. The heat capacity and entropy functions were calculated at selected temperatures between T= (0 and 300) K and are listed in Table A.4.(See Table A.5)

5.4. Mixing properties of the $(K_xTh_{1-x})F_{4-3x}$ liquid solution

The determination of the mixing enthalpy of the liquid solution is very useful in the assessment of a complex system such as KF-ThF_4 as it provides another dataset, besides the phase diagram points, to optimize the excess Gibbs energy terms of the liquid phase. Table 7 reports the values for the mixing enthalpies of the $(K_xTh_{1-x})F_{4-3x}$ liquid solution as determined in this work at the melting temperature of KF, i.e., (1131 ± 10) K. The range of investigated compositions is limited by the large difference in molar masses between the two salts: at high $X(ThF_4)$ mole fraction, the mass of ThF_4 is much larger compared to the mass of the solvent KF, with lower melting temperature, such that complete mixing of liquid KF with ThF_4, is difficult to obtain. However, complete mixing of the liquid solution compositions reported in Table 7 was ensured by the presence of one single event which corresponded to the combination of KF melting, ThF_4 melting, and mixing event, and the absence of other events such as the melting of residual ThF_4, invariant equilibrium reactions, or the liquidus at the given composition. An example of a successful measurement is shown in Fig. A.5.

The experimental data obtained in this work and the curve predicted by our model are plotted for comparison (green) in Fig. 9a against the mixing enthalpies of the LiF-ThF_4 (red), NaF-ThF_4 (blue) and CsF-ThF_4 (black) systems as calculated respectively from the thermodynamic assessments of Capelli et al. [24], Beneš et al. [28] and Vozárová et al. [42]. The present experimental data and modelled mixing enthalpies are more negative than for the LiF-ThF_4 and NaF-ThF_4 systems, which is consistent with the increase in the alkali cation ionic radius. Depending on composition and temperature, liquid fluoride salts can form dissociated ions, molecular species, or even a polymeric network. The larger K^+ ion offers a larger steric hindrance than Li^+ and Na^+, isolating the coordination complexes ThF_n^{4-n} from each other, and therefore stabilizing the coordination shell around Th^{4+}. Evidence of this stability was provided by Pauvert et al. in the analogous AF-ZrF_4 systems [43]. The authors calculated the lifetimes of the Zr^{4+} first solvation shells in LiF-ZrF_4, NaF-ZrF_4, and KF-ZrF_4 melts at X(Zr= $X(ZrF_4)$= 0.35 using molecular dynamics. As in [44,45], they defined the lifetime τ to be the time at which the cage-out correlation function [46] decays to a value of $1/e$. Pauvert et al. found the lifetimes to increase with the ionic radius of the alkali metal (calculated as 3.1, 15.7, and 76.4 ps, respectively). Similarly to the behavior in AF-MCl_2 melts [47], (A = alkali metal, M = transition metal), a coordination complex around Th^{4+} in the $(K,Th)F_x$ liquid solution is also likely to be further stabilized compared to its analogue in $(Li,Th)F_x$ or $(Na,Th)F_x$ liquid solutions due to polarization effects: lighter alkali ions are more polarizing than K^+ and thus are able to attract F^- more strongly, leading to longer - $Th^{4+} - F^-$ distances and weaker complexes. The most negative mixing enthalpy curve, corresponding to the largest cation Cs^+, fits this trend.

Gibbs energies of mixing (Fig. 10a) also reflect this trend in stability, with the composition of maximum stability indicated by the minimum in the curve. This composition is related to the choice of cation-cation coordination numbers (Table 5), as is the maximum

---

[10] The quoted uncertainty corresponds to the standard uncertainty.

Table 9
Invariant equilibrium data in the KF-ThF_4 system.

Equilibrium	Invariant reaction	This study (calc.)		DSC equilib. global average		Emelyanov and Evstyukhin[c] [8]		Asker et al. [9]	
		X(ThF_4)	T/K	X(ThF_4)[a]	T/K[b]	X(ThF_4)	T/K	X(ThF_4)[d]	T/K[e]
Eutectic	$KF + K_5ThF_9\text{-}\beta = L$	0.152	971.8	–	968[k]	–	935	0.14	967
Peritectic	$K_5ThF_9\text{-}\beta = K_3ThF_7 + L$	0.167	973.5[f]	0.167	977[k]	0.167	966	0.14	967
$\alpha - \beta$ transition	$K_5ThF_9\text{-}\alpha = K_5ThF_9\text{-}\beta$	0.167	926	0.167	926[h]	0.167	874[g]	0.167	908
Eutectoid	$K_3ThF_7 = K_5ThF_9\text{-}\alpha + K_2ThF_6\text{-}\alpha$	0.25	844.9	0.25	854[k]	–	–	0.25	843
Congruent melting	$K_3ThF_7 = L$	0.25	1142.8	0.25	1141	0.25	1129	0.25	1138
Eutectic	$K_3ThF_7 + K_2ThF_6\text{-}\beta = L$	0.299	980.3	–	961	0.34	1014	0.31	964
$\alpha - \beta$ transition	$K_2ThF_6\text{-}\alpha = K_2ThF_6\text{-}\beta$	0.333	952	0.333	952	–	936[h]	0.333	918
Peritectic	$K_2ThF_6\text{-}\beta = L + K_7Th_6F_{31}$	0.333	997.2	0.333	1000	–	–	0.333	1020
Congruent melting	$K_7Th_6F_{31} = L$	0.462	1183.4	–	–	0.5	1166	0.5	1178
Eutectic	$K_7Th_6F_{31} + K_2ThF_9 = L$	0.511	1174.9	–	1158[k]	0.54	1133	0.56	1148
Congruent melting	$K_2ThF_9 = L$	0.667	1217.2	0.666	1202	0.666	1173	0.66	1203
Peritectic	$KTh_6F_{25} = ThF_4 + L$	0.857	1224	0.857	1220[k]	0.857	1203	0.78	1253[i]

[j] Interpreted by the authors to be a eutectic.

[a] Standard uncertainties u are u(X(ThF_4))) = 0.05.

[b] Standard uncertainties u are u(T) = 5 K for pure end-members, 10 K for mixtures.

[c] No uncertainties reported for composition or temperature.

[d] ThF_4 reagent is estimated to be 99 % pure, no other composition errors are reported.

[e] Reported standard uncertainties u are u(T) = 5 K for phase transitions and incongruent melting points, no uncertainties reported for liquidus points.

[f] Calculated as congruent melting.

[g] Attributed to be a lower limit of stability.

[h] The authors did not attribute it to any equilibrium.

[i] Interpreted by the authors to be a congruent melting point.

[k] Global average of the experimental runs appearing in Table 8. Measurements done at (0.10 ± 0.01) MPa.

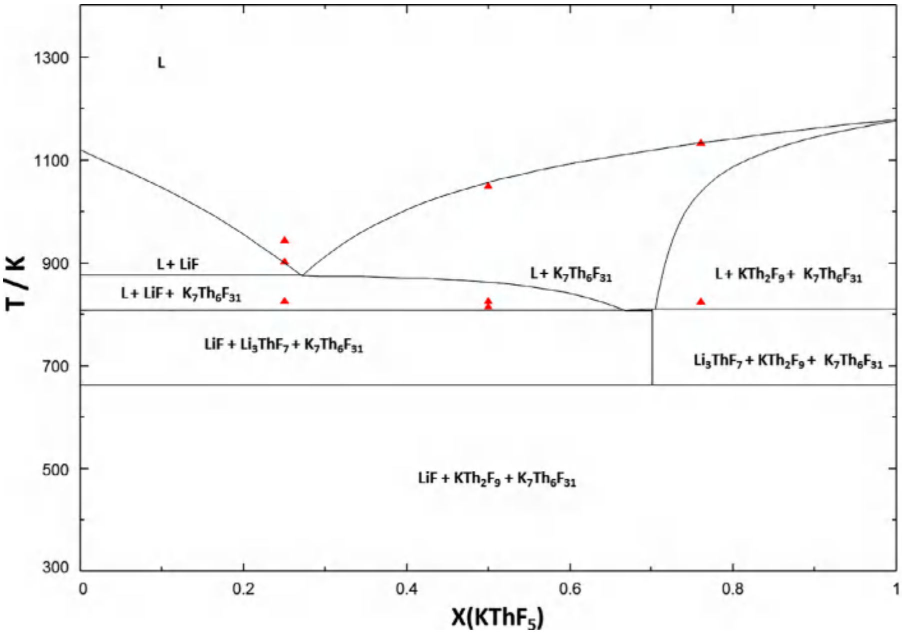

Fig. 12. Phase diagram of the LiF-$KThF_5$ pseudobinary section as calculated in this study superimposed against experimental points measured in this work (▲, red, listed in Table 12). (For interpretation of the references to colour in this figure legend, the reader is referred to the web version of this article.)

of the M-Th-F-F pair fractions (Fig. 10b), which is around X(ThF_4) = 0.25 for Li, Na systems and X(ThF_4) = 0.33 for K, Cs systems. The basicity of the systems can be qualitatively gauged from the shape and value of the M-Th-F-F maximum: a strongly basic system would lead to complete dissociation of the cation-cation pairs to result in perfect SNN ordering, i.e., a bond fraction of unity at the composition of maximum short-range ordering. In this case, the systems can be qualified as moderately to reasonably basic with a round shape for the M-Th-F-F fraction and maximum value between 0.55 and 0.79. Moreover the degree of basicity is closely linked with the stability trend just discussed: the maximum fraction of the Li-Th-F-F distributions is the lowest, those of K-Th-F-F and Cs-Th-F-F are the highest. It is interesting to note that not even CsF-ThF_4 is basic enough for Cs-Th-F-F to reach unity; it can be expected that FrF-ThF_4 would come closest.

The entropies of mixing are plotted in Fig. 9b. Capelli et al. [16] related the maximum for mixing entropy in LiF-ThF_4 at X(ThF4) ≈ 0.25 to a higher content of free F^-, observed in NMR studies by Bessada et al. [48]. The computed curves suggest that there would be less free F^-, at least in the KF and CsF-based systems. Structural studies such as NMR or EXAFS on these systems at high ThF_4 compositions could help understand if this trend is correct.

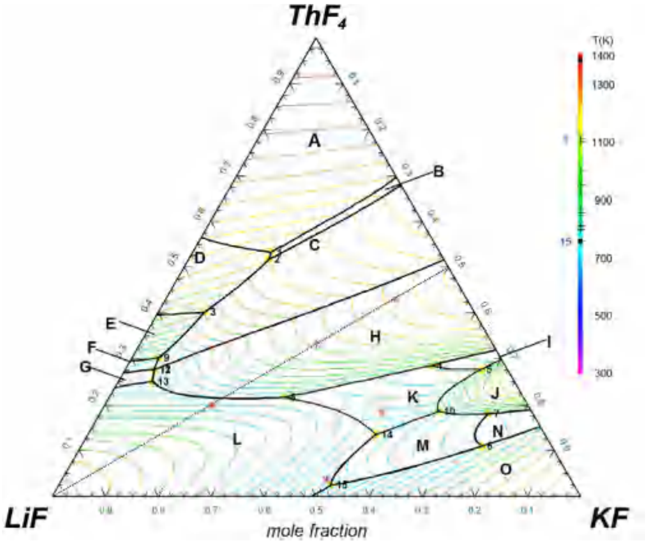

Fig. 13. Liquidus projection and primary crystallization fields in the LiF-KF-ThF_4 system as calculated in this study. The spacing between the isotherms is 25 K. The dashed line represents the LiF-$KThF_5$ pseudobinary section shown in Fig. 12. Experimental points: (✱). Primary crystallization phase fields: (A) ThF_4(s); (B) KTh_6F_{25}; (C) KTh_2F_9; (D) $LiTh_4F_{17}$; (E) $LiTh_2F_9$; (F) $LiThF_5$; (G) Li_3ThF_7; (H) $K_7Th_6F_{31}$; (I) β-K_2ThF_6; (J) K_3ThF_7; (K) α-K_2ThF_6; (L) LiF; (M) α-K_5ThF_9; (N) β-K_5ThF_9; (O) KF.

5.5. CALPHAD assessment of the KF-ThF_4 system

The KF-ThF_4 system (Fig. 11) was finally optimized based on our measured DSC equilibrium and mixing enthalpy data, all of which are presented in Table 8.There are 6 intermediate compounds: K_5UF_9 (α and β phases), K_3ThF_7, K_2ThF_6 (α and β phases), $K_7Th_6F_{31}$, KTh_2F_9, and KTh_6F_{25}. The phase diagram is further characterized by four eutectics ($X(ThF_4)$ = 0.152, 0.298, 0.511, 0.681), three peritectics ($X(ThF_4)$ = 0.165, 0.333, 0.743), three congruent melting points ($X(ThF_4)$ = 0.25, 0.462, 0.667), and two limits of stability ($X(ThF_4)$ = 0.25, 0.333); the temperatures and compositions of these equilibria are listed in Table 9. It can be seen that the liquidus temperatures measured in this work are sometimes slightly higher than those reported by the previous studies. This is most likely because the authors [9,8] used onset temperatures rather than minimum temperatures on the heat flow events for liquidus determination (see Fig. A.3 for an explanation of how these are determined in this work in a typical DSC measurement). In fact, the agreement with the previous studies [8,9] becomes much better if the onset temperatures of the liquidus equilibria as measured in this work (▽, red) are selected (see Fig. 11).

5.6. CALPHAD assessment of the LiF-KF-ThF_4 system

5.6.1. LiF-$KThF_5$ pseudobinary section

Some equilibrium data were collected along the LiF-$KThF_5$ pseudobinary section in order to optimize the liquidus surface of the LiF-KF-ThF_4 ternary system. The section is relatively simple, as shown in Fig. 12. LiF is the first compound to crystallize below 25 mol ∼ 25 mol % $X(KThF_5)$, beyond that the liquid solution is in equilibrium with $K_7Th_6F_{31}$. Below the solidus the calculation shows that there are two ternary phase fields throughout the composition range: {LiF + Li_3ThF_7 + $K_7Th_6F_{31}$} and {Li_3ThF_7 + KTh_2F_9 + $K_7Th_6F_{31}$}. Below ∼662 K the equilibrium is between LiF, KTh_2F_9, and $K_7Th_6F_{31}$. The experimental points, however, suggest that the temperature range in which {LiF + Li_3ThF_7 + $K_7Th_6F_{31}$} and {Li_3ThF_7 + KTh_2F_9 + $K_7Th_6F_{31}$} exist is much more narrow. The phase equilibria of the experimental points are given in Table 12.

5.6.2. LiF-KF-ThF_4 liquidus projection

The LiF-KF-ThF_4 system (Fig. 13) as calculated in this study is characterized by fifteen primary fields of crystallization and nineteen invariant points: nine quasi-peritectics, four saddle points, two peritectics, and four eutectics, the lowest of which is calculated at T = 755 K, very close to the LiF-KF eutectic: ($X(ThF_4)$, X(LiF), X(KF)) = (0.023, 0.461, 0.516). DSC analysis of an experimental point in the neighborhood of this ternary eutectic ($X(ThF_4)$, X(LiF), X(KF)) = (0.037, 0.463, 0.500) showed only one event at T = (753 ± 10 K), which can be assigned to the invariant reaction LiF(cr) + KF(cr) + K_5ThF_9(cr) = L. Hence, the point is a ternary eutectic. The agreement between the measured and calculated liquidus points is reported in Table 10. The solid phases in equilibrium with the liquid, compositions, and temperatures of all calculated invariant equilibria are listed in Table 10. The rest of the equilibria measured by DSC are listed in Table 11. There are no ternary stoichiometric compounds or solid solutions in the ternary system reported in the literature.

5.7. CALPHAD assessment of the NaF-KF-ThF_4 system

5.7.1. NaF-$KThF_5$ pseudobinary section

The NaF-$KThF_5$ pseudobinary section, studied by Emelyanov and Evstyukhin, is the only set of data reported in the literature related to the liquidus surface of the NaF-KF-ThF_4 ternary system. As measured by the authors, the pseudo-binary section shows only one intermediate compound: the quaternary fluoride $KNaThF_6$, displaying a phase transition at 813 K [8], and incongruent melting at 938 K. In this work the $\alpha - \beta$ transition of $KNaThF_6$ was observed at (825 ± 10) K. The enthalpy of transition was measured to be $\Delta_{tr}H^o_m = (15.3 \pm 0.6)\ \mathrm{kJ{\cdot}mol^{-1}}$. The melting event was observed at (940 ± 10) K. The authors reported a peritectic decomposition, which agrees with the phase transition predicted by our calculation, namely

$$\beta - KNaThF_6 \longrightarrow K_7Th_6F_{31} + L \tag{22}$$

In our calorimetric measurement we were not able to detect a third event which would correspond to the liquidus, and neither did [8] (Fig. 14). This might be due to a very close proximity of the incongruent melting event to the liquidus surface, making it hard to detect.

Table 10

Calculated vs. experimental liquidus temperatures in the LiF-KF-ThF_4 system.

$X(ThF_4)^a$	$X(LiF)^a$	$X(KF)^a$	Equilibrium reaction	T_{calc}/K	$T_{exp}{}^b$/K
0.037	0.463	0.500	LiF + KF + α-K_5ThF_9 = L	783^c	753^d
0.183	0.285	0.532	K_2ThF_6-α + L′ = L	866	839
0.430	0.138	0.432	$K_7Th_6F_{31}$ + L′ = L	1133	1133
0.200	0.597	0.203	LiF + L′ = L	901	943
0.333	0.334	0.333	$K_7Th_6F_{31}$ + L′ = L	1056	1050

[a] Standard composition error is $u(\|(X(ThF_4), X(LiF), X(KF))\|)$ = 0.006.
[b] Standard uncertainties u are u(T)=10 K.
[c] Calculated as LiF + L′ = L at the experimental composition, since the eutectic does not exactly match the experimental one.
[d] Eutectic temperature calculated as 755 K in the vicinity of the experimental composition, see Table 11. Measurements done at (0.10 ± 0.01) MPa.

Table 11
Invariant equilibrium data and saddle points calculated in the LiF-KF-ThF$_4$ system.

X(ThF$_4$)	X(LiF)	X(KF)	T$_{calc}$/K	Equilibrium	Solid phases present
0.533	0.319	0.148	1113.5	Quasi-peritectic	KTh_6F_{25} + $LiTh_4F_{17}$ + ThF_4
0.517	0.331	0.152	1101.4	Quasi-peritectic	KTh_2F_9 + KTh_6F_{25} + $LiTh_4F_{17}$
0.402	0.510	0.088	1003.2	Quasi-peritectic	KTh_2F_9 + $LiTh_2F_9$ + $LiTh_4F_{17}$
0.285	0.140	0.575	952.0	Peritectic	α-K_2ThF_6 + β-K_2ThF_6 + $K_7Th_6F_{31}$
0.276	0.049	0.674	952.0	Quasi-peritectic	α-K_2ThF_6 + β-K_2ThF_6 + K_3ThF_7
0.109	0.131	0.760	926.0	Peritectic	KF + α-K_5ThF_9 + β-K_5ThF_9
0.165	0.103	0.732	926.1	Saddle point	α-K_5ThF_9 + β-K_5ThF_9
0.180	0.084	0.736	926.0	Quasi-peritectic	α-K_5ThF_9 + β-K_5ThF_9 + K_3ThF_7
0.214	0.827	0.286	879.5	Saddle point	$K_7Th_6F_{31}$ + LiF
0.194	0.390	0.416	877.6	Saddle point	$K_7Th_6F_{31}$ + LiF
0.215	0.451	0.334	869.0	Eutectic	α-K_2ThF_6 + $K_7Th_6F_{31}$ + LiF
0.302	0.647	0.051	852.9	Quasi-peritectic	KTh_2F_9 + $LiTh_2F_9$ + $LiThF_5$
0.185	0.176	0.639	846.4	Quasi-peritectic	α-K_2ThF_6 + K_3ThF_7 + α-K_5ThF_9
0.276	0.669	0.054	810.2	Quasi-peritectic	KTh_2F_9 + Li_3ThF_7 + $LiThF_5$
0.275	0.669	0.054	809.9	Quasi-peritectic	$K_7Th_6F_{31}$ + KTh_2F_9 + Li_3ThF_7
0.251	0.685	0.064	807.7	Eutectic	$K_7Th_6F_{31}$ + Li_3ThF_7 + LiF
0.107	0.355	0.538	803.7	Saddle point	LiF + α-K_5ThF_9
0.135	0.319	0.546	797.7	Eutectic	α-K_2ThF_6 + α-K_5ThF_9 + LiF
0.023	0.461	0.516	754.8	Eutectic	α-K_5ThF_9 + KF + LiF

Table 12
Phase diagram equilibria of the LiF-KF-ThF$_4$ system as measured in this study by DSC.

X(ThF$_4$)[a]	X(LiF)[a]	X(KF)[a]	T$_{exp}$/K[b]	Equilibrium	Equilibrium Reaction
0.037	0.463	0.500	753	Eutectic	LiF + KF + α-K_5ThF_9 = L
0.183	0.285	0.532	816	Eutectic	LiF + α-K_5ThF_9 + α-K_2ThF_6 = L
			839	Liquidus	α-K_2ThF_6 + L′ = L
0.430	0.138	0.432	825	Eutectic	Li_3ThF_7 + $K_7Th_6F_{31}$ + KTh_2F_9 = L
			1133	Liquidus	$K_7Th_6F_{31}$ + L′ = L
0.200	0.597	0.203	826	Eutectic	LiF + Li_3ThF_7 + $K_7Th_6F_{31}$ = L
			902	Quasi-peritectic	L′ + LiF + $K_7Th_6F_{31}$ = L + LiF
			943	Liquidus	LiF + L′ = L
0.333	0.334	0.333	815	Eutectoid	Li_3ThF_7 + $K_7Th_6F_{31}$ = LiF + KTh_2F_9
			825	Eutectic	Li_3ThF_7 + $K_7Th_6F_{31}$ + LiF = L
			1050	Liquidus	$K_7Th_6F_{31}$ + L′ = L

[a] Standard composition error is $u(\|(X(ThF_4), X(LiF), X(KF))\|) = 0.006$.
[b] Standard uncertainties u are $u(T)$=10 K. The pressure was (0.10 ± 0.01) MPa.

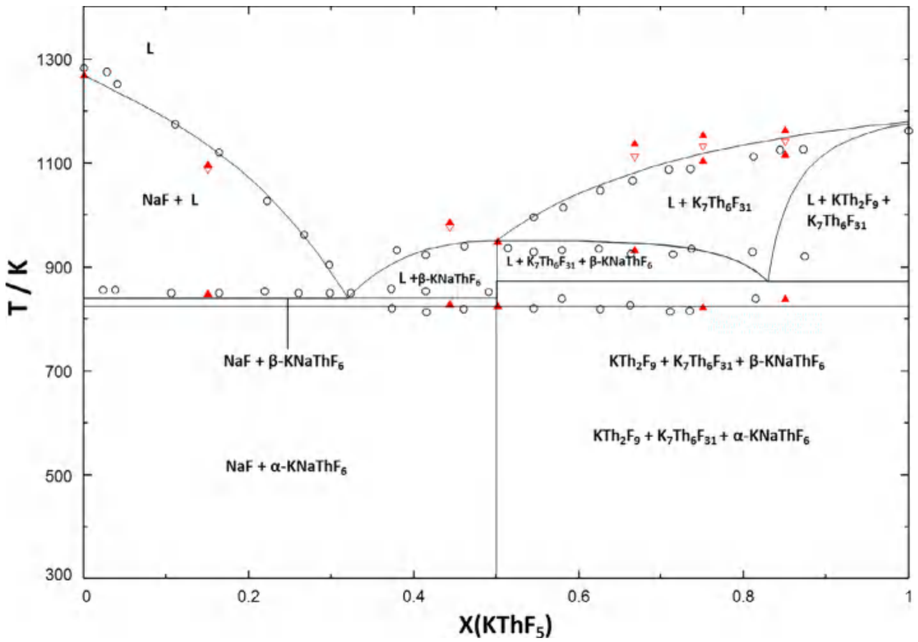

Fig. 14. Phase diagram of the NaF-KThF$_5$ pseudobinary section as calculated in this study superimposed against experimental points by Emelyanov and Evstyukhin [8], (•, black) and experimental points measured in this work (▲, liquidus onset ▽, red, included in Table 16). (For interpretation of the references to colour in this figure legend, the reader is referred to the web version of this article.)

Table 13
Projection of the NaF-KF-ThF_4 system at 300 K.

Set of points	Experimentally observed phases by [8]	Calculated phases, this study
red circles	NaF + K_3ThF_7 + KF	NaF + K_5ThF_9 + $KNaThF_6$
blue triangles	NaF + $K_3Th_2F_{11}$ + K_3ThF_7	NaF + K_5ThF_9 + $KNaThF_6$/K_2ThF_6 + $KNaThF_6$ + K_5ThF_9
black squares	unidentified lines	NaF + K_5ThF_9 + $KNaThF_6$/$KNaThF_6$ + K_2ThF_6
green diamonds	NaF + $KNaThF_6$	NaF + $KNaThF_6$
half-filled squares	phase similar to $KNaThF_6$ and unidentified lines	NaF + K_5ThF_9 + $KNaThF_6$
half-filled circle	$KNaThF_6$	$KNaThF_6$
black circle	$KNaThF_6$ + $KThF_5$	KTh_2F_9 + $K_7Th_6F_{31}$ + $KNaThF_6$
half-filled diamond	$KThF_5$ + $KNaThF_6$ + unidentified lines	$NaThF_5$ + Na_2ThF_6 + $KNaThF_6$/$NaThF_5$ + KTh_2F_9 + $KNaThF_6$
half-filled orange triangle	Na_2ThF_6 + unidentified lines	NaF + Na_2ThF_6 + $KNaThF_6$/Na_2ThF_6 + $KNaThF_6$
filled orange triangle	Na_2ThF_6 + $KNaThF_6$	NaF + Na_2ThF_6 + $KNaThF_6$
empty orange triangle	Na_2ThF_6 + $KNaThF_6$ + Na_4ThF_8(?)	NaF + Na_2ThF_6 + $KNaThF_6$
white circle	$KNaThF_6$ + weak lines	NaF + Na_2ThF_6 + $KNaThF_6$

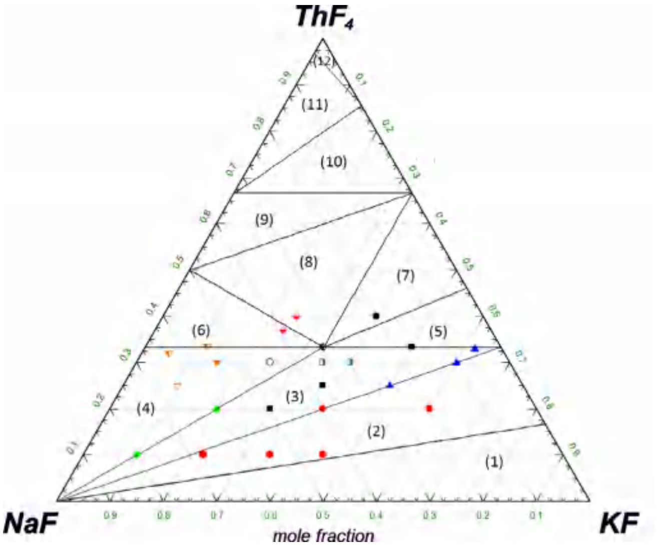

Fig. 15. Projection of the NaF-KF-ThF_4 ternary system as calculated in this study at 300 K superimposed against experimental compositions analyzed using XRD by [8]: red circles: {NaF + K_3ThF_7 + KF}; blue triangles: {NaF + $K_3Th_2F_{11}$ + K_3ThF_7}; black squares: unidentified patterns; green diamonds: {NaF + $KNaThF_6$}; half-filled squares: phase similar to $KNaThF_6$ and unidentified lines; half-filled circle: {$KNaThF_6$}; black circle: {$KNaThF_6$ + $KThF_5$}; half-filled diamond: {$KThF_5$ + $KNaThF_6$ + unidentified lines}; half-filled orange triangle: {Na_2ThF_6 + unidentified lines}; filled orange triangle:{Na_2ThF_6 + $KNaThF_6$}; empty orange triangle: {Na_2ThF_6 + $KNaThF_6$ + Na_4ThF_8(?)}; white circle: {$KNaThF_6$ + weak lines}. These data are also compared in Table 13 for more clarity. Phases in equilibrium in phase fields (1)-(11) are listed in Section 5.7.2. (For interpretation of the references to colour in this figure legend, the reader is referred to the web version of this article.)

5.7.2. Phase Equilibria at 300 K

In addition to the section of the liquidus surface which can be observed along the NaF-$KThF_5$ pseudobinary section, Emelyanov and Evstyukhin [8] analyzed several melts of the ternary phase diagram at room temperature using XRD to determine their phase composition, reported in Table 13. These are compared to the equilibrium phase fields as calculated herein. The authors concluded that within this region of the phase diagram there are six equilibrium ternary phase fields having the following compositions:

(a) NaF + K_3ThF_7+ KF
(b) NaF + $K_3Th_2F_{11}$+ K_3ThF_7
(c) NaF + $KNaThF_6$+ $K_3Th_2F_{11}$
(d) NaF + Na_2ThF_6+ $KNaThF_6$
(e) Na_2ThF_6+ $KNaThF_6$+ $KThF_5$
(f) $KNaThF_6$+ $KThF_5$+ $K_3Th_2F_{11}$

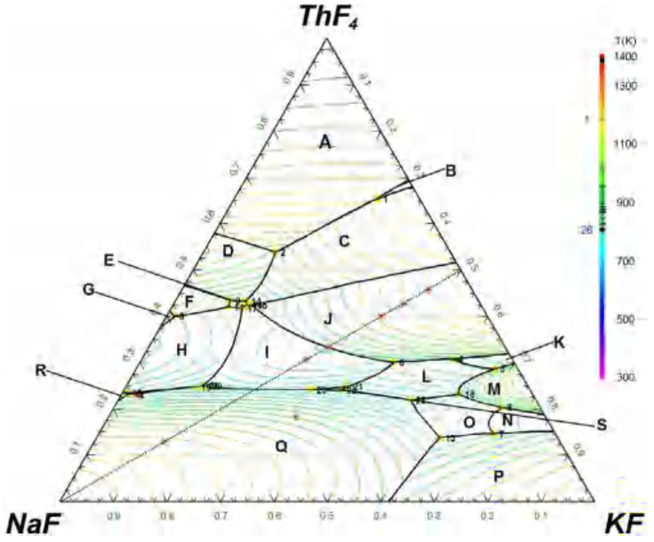

Fig. 16. Liquidus projection and primary crystallization fields of the NaF-KF-ThF_4 system as calculated in this study. The spacing between the isotherms is 25 K. Experimental points: (*). The dashed line is the pseudobinary section shown in Fig. 14. Primary crystallization phase fields: (A) $(Na_xTh_{1-x})F_{4-3x}$; (B) KTh_6F_{25}; (C) KTh_2F_9; (D) $NaTh_2F_9$; (E) $NaThF_5$; (F) $Na_7Th_6F_{31}$; (G) $Na_3Th_2F_{11}$; (H) Na_2ThF_6; (I) β-$KNaThF_6$; (J) $K_7Th_6F_{31}$; (K) β-K_2ThF_6; (L) α-K_2ThF_6; (M) K_3ThF_7; (N) β-K_5ThF_9; (O) α-K_5ThF_9; (P) (Na,K) F; (Q) NaF; (R) Na_4ThF_8; (S) α-$KNaThF_6$.

In the present assessment 12 ternary phase fields are calculated (Fig. 15):

1. NaF + (Na,K)F + K_5ThF_9
2. NaF + K_2ThF_6+ K_5ThF_9
3. NaF + K_2ThF_6+ $KNaThF_6$
4. NaF + Na_2ThF_6+ $KNaThF_6$
5. K_2ThF_6+ $K_7Th_6F_{31}$ + $KNaThF_6$
6. $NaThF_5$+ Na_2ThF_6+ $KNaThF_6$
7. KTh_2F_9+ $K_7Th_6F_{31}$ + $KNaThF_6$
8. $NaThF_5$+ KTh_2F_9+ $KNaThF_6$
9. $NaThF_5$+ KTh_2F_9+ KTh_2F_9
10. $NaThF_5$+ KTh_2F_9+ KTh_6F_{25}
11. $Na_xTh_{1-x}F_{4-3x}$ + $NaTh_2F_9$+ KTh_6F_{25}
12. $Na_xTh_{1-x}F_{4-3x}$ + KTh_6F_{25}

Among these, (2)-(8) are found within the region studied by the authors. The main differences can be related to those already discussed in the KF-ThF_4 binary phase diagram: [8] observed K_3ThF_7 in fields (a) and (b). We find this compound to decompose around

Table 14
Invariant equilibrium data calculated in the NaF-KF-ThF_4 system.

X(ThF_4)	X(NaF)	X(KF)	T_{calc}/K	Equilibrium	Solid phases present
0.654	0.078	0.268	1185.3	Quasi-peritectic	KTh_6F_{25} + KTh_2F_9 + $(Na_xTh_{1-x})F_{4-3x}$
0.538	0.327	0.135	1017.7	Quasi-peritectic	KTh_2F_9 + $NaTh_2F_9$ + $(Na_xTh_{1-x})F_{4-3x}$
0.399	0.587	0.014	954.7	Quasi-peritectic	Na_2ThF_6 + $Na_3Th_2F_{11}$ + $Na_7Th_6F_{31}$
0.301	0.100	0.599	952.9	Saddle point	α-K_2ThF_6 + β-K_2ThF_6
0.308	0.112	0.580	952.0	Quasi-peritectic	α-K_2ThF_6 + β-K_2ThF_6 +$K_7Th_6F_{31}$
0.285	0.044	0.671	952.0	Quasi-peritectic	α-K_2ThF_6 + β-K_2ThF_6 +K_3ThF_7
0.187	0.093	0.720	927.9	Saddle point	α-K_5ThF_9 + β-K_5ThF_9
0.204	0.071	0.725	926.0	Peritectic	α-K_5ThF_9 + β-K_5ThF_9 + K_3ThF_7
0.147	0.114	0.739	926.0	Quasi-peritectic	α-K_5ThF_9 + β-K_5ThF_9 + (Na,K) F
0.300	0.225	0.475	909.2	Peritectic	$K_7Th_6F_{31}$ + β-$KNaThF_6$ + α-K_2ThF_6
0.331	0.511	0.158	900.1	Saddle point	Na_2ThF_6 + β-$KNaThF_6$
0.434	0.465	0.101	892.8	Peritectic	$Na_7Th_6F_{31}$ + $NaTh_2F_9$ + $NaThF_5$
0.233	0.759	0.008	884.3	Quasi-peritectic	Na_2ThF_6 + Na_4ThF_8 + $Na_7Th_2F_{1}5$
0.421	0.474	0.105	883.2	Quasi-peritectic	Na_2ThF_6 + $Na_7Th_6F_{31}$ + $NaThF_5$
0.231	0.756	0.013	883.0	Quasi-peritectic	Na_4ThF_8 + $Na_7Th_2F_{1}5$ + NaF
0.138	0.220	0.642	882.5	Quasi-peritectic	NaF + $\alpha - K_5ThF_9$ + (Na,K) F
0.432	0.436	0.132	873.4	Quasi-peritectic	KTh_2F_9 + $NaTh_2F_9$ + $NaThF_5$
0.242	0.535	0.223	842.0	Saddle point	β-$KNaThF_6$ + NaF
0.424	0.429	0.147	872.9	Quasi-peritectic	KTh_2F_9 +$K_7Th_6F_{31}$ + β-$KNaThF_6$
0.425	0.437	0.138	866.2	Quasi-peritectic	$NaThF_5$ + KTh_2F_9 + β-$KNaThF_6$
0.418	0.450	0.132	865.4	Quasi-peritectic	$NaThF_5$ +Na_2ThF_6 + β-$KNaThF_6$
0.232	0.137	0.631	846.2	Quasi-peritectic	α-K_2ThF_6 + $\alpha - K_5ThF_9$ + K_3ThF_7
0.231	0.300	0.469	816.3	Saddle point	α-K_2ThF_6 + NaF
0.247	0.624	0.1129	829.2	Quasi-peritectic	Na_2ThF_6 + $Na_7Th_2F_{15}$ + NaF
0.248	0.337	0.415	825.0	Peritectic	α-$KNaThF_6$ + β-$KNaThF_6$ + α-K_2ThF_6
0.250	0.606	0.144	825.0	Quasi-peritectic	α-$KNaThF_6$ + NaF + β-$KNaThF_6$
0.248	0.601	0.151	825.0	Quasi-peritectic	α-$KNaThF_6$ + NaF + β-$KNaThF_6$
0.241	0.411	0.348	825.0	Eutectic	α-$KNaThF_6$ + β-$KNaThF_6$ + NaF
0.249	0.608	0.143	822.1	Eutectic	α-$KNaThF_6$ + Na_2ThF_6 + NaF
0.241	0.353	0.406	808.1	Quasi-peritectic	α-$KNaThF_6$ + α-K_2ThF_6 + NaF
0.219	0.234	0.547	804.3	Eutectic	α-K_2ThF_6 + $\alpha - K_5ThF_9$ + NaF

Table 15
Calculated vs. experimental liquidus temperatures in the NaF-KF-ThF_4 system.

X(ThF_4)[a]	X(NaF)[a]	X(KF)[a]	Equilibrium Reaction	T_{calc}/K	T_{exp}[b]/K
0.307	0.386	0.307	L′ + β-$KNaThF_6$ = L	943	986
0.130	0.739	0.131	NaF + L′ = L	1133	1096
0.230	0.741	0.029	NaF + L′ = L	893	888
0.334	0.332	0.334	L′ + $K_7Th_6F_{31}$ = L	950	–
0.183	0.467	0.350	NaF + L′ = L	995	977
0.401	0.199	0.400	L′ + $K_7Th_6F_{31}$ = L	1082	1136
0.428	0.143	0.430	L′ + $K_7Th_6F_{31}$ = L	1117	1153
0.459	0.082	0.459	L′ + $K_7Th_6F_{31}$ = L	1148	1163

[a] Standard composition error is $u(||(X(ThF_4), X(NaF), X(KF))||) = 0.006$.

[b] Standard uncertainties u are u(T)=10 K. The pressure was (0.10 ± 0.01) MPa.

979 K, however, and so we predict K_5ThF_9 to be the stable phase instead. In experimental points represented by (half-filled square) they reported unidentified lines, which possibly were those of K_5ThF_9. Similarly, they observed phase fields with $K_3Th_2F_{11}$ whereas our model predicts the phase K_2ThF_6. Fields (d) and (4) coincide fully, but again e) disagrees with our calculation having established that $KThF_5$ is not a true stable phase. However, our model does predict that $K_7Th_6F_{31}$ exists in those regions where they reported $KThF_5$ to be present. Finally, phase fields (f) and (5) also coincide fully allowing for the fact that the authors misinterpreted XRD patterns of $KThF_5$ and $K_3Th_2F_{11}$ with those of $K_7Th_6F_{31}$ and K_2ThF_6, respectively. The only compound in the region of interest which was not reported by them but which appears in our projection is $NaThF_5$, which was possibly observed given that points represented by (half-filled diamond) showed Bragg reflections they could not identify. Overall, the agreement is close enough to consider the description of solid equilibra as satisfactory.

5.7.3. NaF-KF-ThF_4 liquidus projection

The NaF-KF-ThF_4 (Fig. 16) system is an even more complex system, with one quaternary compound (displaying a phase transition), 19 primary crystallization fields and 31 invariant points (Table 14). Of these, nineteen are quasi-peritectic, five are saddle points, four are peritectic, and four are eutectic, with the lowest one occurring at 804 K and X(ThF_4) = (0.219, 0.234, 0.547). We have found the liquidus temperatures of eight samples (points shown in red) to closely match the calculated ones only in most instances (Table 15). All equilibria measured experimentally are given in Table 16.

6. Conclusions

A thermodynamic assessment for the KF-ThF_4 binary system using the CALPHAD method is reported for the first time in combination with XRD and calorimetric measurements. The main char-

Table 16
Phase diagram equilibria of the NaF-KF-ThF$_4$ system as measured in this study by DSC.

X(ThF$_4$)[a]	X(NaF)[a]	X(KF)[a]	T_{exp}/K[b]	Equilibrium	Equilibrium Reaction
0.307	0.386	0.307	827	KNaThF$_6$ transition	α-K$_2$ThF$_6$ = β-K$_2$ThF$_6$
			986	Liquidus	L′ + β-KNaThF$_6$ = L
0.130	0.739	0.131	848	Eutectic	NaF + β-KNaThF$_6$ = L
			1096	Liquidus	NaF + L′ = L
0.230	0.741	0.029	802	Eutectoid	Na$_7$Th$_2$F$_{15}$ = NaF + Na$_2$ThF$_6$
			888	Liquidus	NaF + L′ = L
0.334	0.332	0.334	825	KNaThF$_6$ transition	α-K$_2$ThF$_6$ = β-K$_2$ThF$_6$
			948	Peritectic	β-K$_2$ThF$_6$ = L + K$_7$Th$_6$F$_{31}$
0.183	0.467	0.350	819	KNaThF$_6$ transition	α-K$_2$ThF$_6$ = β-K$_2$ThF$_6$
			866	K$_2$ThF$_6$ transition	α-K$_2$ThF$_6$ = β-K$_2$ThF$_6$
			977	Liquidus	NaF + L′ = L
0.401	0.199	0.400	931	Peritectic	β-K$_2$ThF$_6$ = L + K$_7$Th$_6$F$_{31}$
			1136	Liquidus	L′ + K$_7$Th$_6$F$_{31}$ = L
0.428	0.143	0.430	821	KNaThF$_6$ transition	α-KNaThF$_6$ = β-KNaThF$_6$
			1104	Quasi-peritectic	L′ + KTh$_2$F$_9$ + K$_7$Th$_6$F$_{31}$ = L + K$_7$Th$_6$F$_{31}$
			1153	Liquidus	L′ + K$_7$Th$_6$F$_{31}$ = L
0.459	0.080	0.459	839	KNaThF$_6$ transition	α-K$_2$ThF$_6$ = β-K$_2$ThF$_6$
			1116	Quasi-peritectic	L′ + KTh$_2$F$_9$ + K$_7$Th$_6$F$_{31}$ = L + K$_7$Th$_6$F$_{31}$
			1163	Liquidus	L′ + K$_7$Th$_6$F$_{31}$ = L

[a] Standard composition error is $u(||(X(ThF_4), X(NaF), X(KF))||) = 0.006$.
[b] Standard uncertainties u are u(T) = 10 K. The pressure was (0.10 ± 0.01) MPa.

acteristics of the sytem are: i) two allotropes of K$_5$ThF$_9$, ii) formation of K$_2$ThF$_6$, with both low and high temperature phases, instead of K$_3$Th$_2$F$_{11}$ as reported earlier [8], iii) a eutectoid decomposition for K$_3$ThF$_7$ at 856 K, iv) existence of the K$_7$Th$_6$F$_{31}$ phase instead of KThF$_5$ as previously reported [9,8], v) congruent melting of KTh$_2$F$_9$, vi) existence of KTh$_6$F$_{25}$ instead of KTh$_3$F$_{13}$ as reported earlier [9], vii) no formation of solid solution. This new assessment, coupled with existing assessments of the LiF-KF, LiF-ThF$_4$, NaF-KF, and NaF-ThF$_4$ systems, was used to extrapolate and optimize the LiF-KF-ThF$_4$ and NaF-KF-ThF$_4$ ternary systems. The lowest melting point in the LiF-KF-ThF$_4$ system is calculated at (X(ThF$_4$, X(LiF), (X(KF)) = (0.023, 0.461, 0.516), T = 755 K. The lowest eutectic temperature in the NaF-KF-ThF$_4$ system is predicted to be 804 K, at composition (X(ThF$_4$, X(NaF), (X(KF)) = (0.219,0.234,0.547).

CRediT author statement

J.A. Ocádiz-Flores :Conceptualization, Methodology, Formal analysis, Investigation, Data Curation, Writing - Original Draft preparation, Visualization **E. Carré** :Data Curation, Investigation **J.-C. Griveau** : Investigation **E. Colineau** : Investigation E. Capelli: Verification **P. Souček** : Resources **O. Beneš** : Resources, Writing-Review & Editing **R.J.M. Konings** :Writing - Review & Editing **A.L. Smith** :Conceptualization, Resources, Writing - Review & Editing, Supervision, Project Administration, Funding acquisition.

Declaration of Competing Interest

The authors declare that they have no known competing financial interests or personal relationships that could have appeared to influence the work reported in this paper.

Acknowledgements

A.L. Smith acknowledges financial support from the Netherlands Organisation for Scientific Research (NWO) (project 722.016.005).

Appendix A. Previous phase diagrams of KF-ThF$_4$ reported in the literature

Figs. A.1 and A.2 show the KF-ThF$_4$ phase diagram as reported by [9] and [8], respectively.

Appendix B. Thermodynamic data for KNaThF$_6$

As mentioned in Section 3, Mukherjee and Dash characterized the properties of KNaThF$_6$ by means of DSC to derive the heat

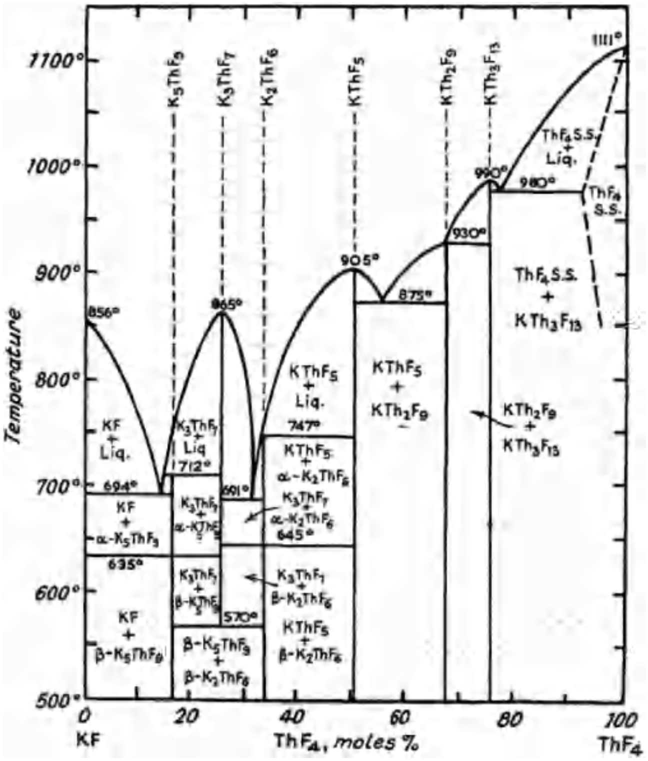

Fig. A.1. KF-ThF$_4$ phase diagram reported by Asker et al. [9], reproduced with permission from the Royal Society of Chemistry.

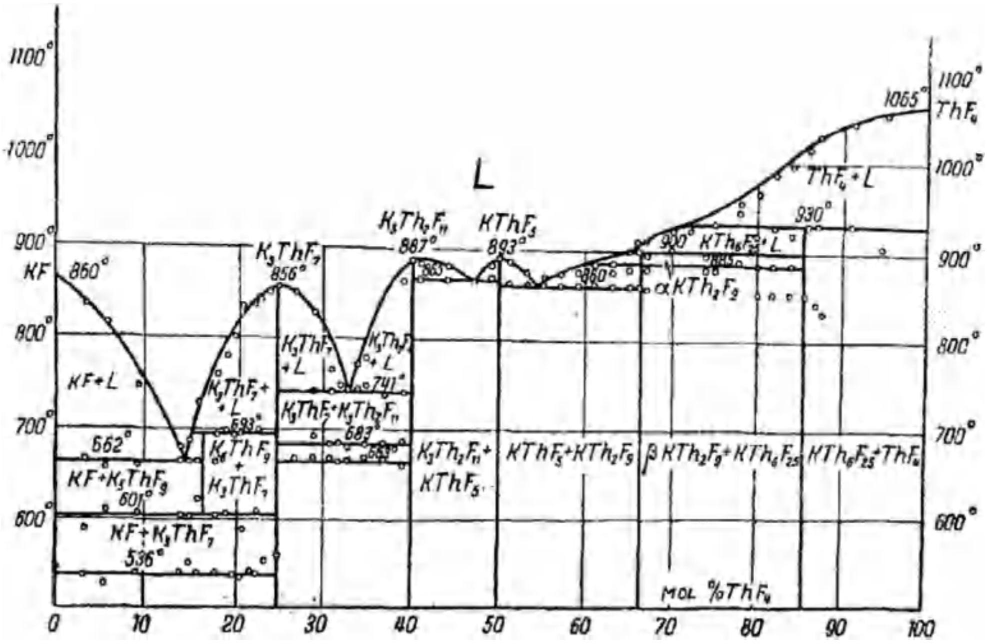

Fig. A.2. KF-ThF_4 phase diagram reported by Emelyanov and Evstyukhin [8]. Reproduced with permission from Springer.

Table A.1
Standard molar Gibbs energies of formation of compounds in Eq. (A.4) expressed as $\Delta_f G^o_m(T)$ (kJ·mol^{-1}) = $A + B \cdot T(K)$.

Compound	A/kJ·mol^{-1}	B/kJ·K^{-1} · mol^{-1}
$ThOF_2$	−1654.7	0.232
NaF	−575.7	0.1026
KF	−567.9	0.1012
NiF_2	−655.05	0.155
NiO	−238.33	0.0918

capacity and solid electrolyte galvanic cell to derive the Gibbs energy of formation [25]. Herein we describe our recalculation of the standard enthalpy of formation and standard entropy based on the data published by the authors [25] and carefully selected auxiliary data.

The solid electrolyte galvanic cell used by Mukherjee and Dash can be described by:

$$(-)Pt,\{ThOF_2(cr) + KNaThF_6(cr) + NaF(cr) + KF(cr)\}|CaF_2(cr)|\{NiO(cr) + NiF_2(cr)\},Pt(+) \quad (A.1)$$

The reaction at the cathode is:

$$NiF_2(cr) + \frac{1}{2}O_{2(g)} + 2e^- = NiO(cr) + 2F^- \quad (A.2)$$

and at the anode:

$$KF(cr) + NaF(cr) + ThOF_2(cr) + 2F^- = KNaThF_6(cr) + \frac{1}{2}O_{2(g)} + 2e^- \quad (A.3)$$

with the net reaction being:

$$KF(cr) + NaF(cr) + ThOF_2(cr) + NiF_2(cr) = KNaThF_6(cr) + NiO(cr) \quad (A.4)$$

The authors measured the electromotive force (e.m.f) as a function of temperature and found linear relationships with two different slopes, corresponding to the two phases of $KNaThF_6(cr)$ [25]: one in the interval 773-848 K and one in the interval 848-973 K. In the lower temperature range of 773-848 K, the following expression was reported:

$$E(T)/V \pm 0.0014 = 0.2772 - 1.586 \cdot 10^{-5} \cdot (T/K)\ (773-848)K \quad (A.5)$$

with the associated Gibbs energy of reaction given by:

$$\Delta_r G^o_m(T) \pm 0.02\,kJ\,mol^{-1} = -53.5 + 0.031 \cdot (T/K)\ (773-848)K \quad (A.6)$$

Table A.2
Experimental lattice parameters of pure phases and mixtures obtained with Rietveld or LeBail refinements at 0.10 ± 0.005 MPa. RT = (293 ± 5) K.

Phases	Composition[a]	a^b/nm	b^b/nm	c^b/nm	α, β, γ °	Space Group	Density[c]/g · cm^{-3}	Literature data/g · cm^{-3}
K_5ThF_9	X(ThF_4) = 0.167	0.7848	1.2840	1.0785	$\alpha = \beta = \gamma = 90$	$Cmc2_1$	3.66 ± 0.01	3.66 [32]
K_5ThF_9	X(ThF_4) = 0.25	0.7846	1.2858	1.0780	$\alpha = \beta = \gamma = 90$	$Cmc2_1$	3.66 ± 0.01	3.66 [32]
K_2ThF_6	X(ThF_4) = 0.25	0.6596	0.6596	0.3862	$\alpha = \beta = 90, \gamma = 120$	$P\bar{6}2$ m	4.84 ± 0.02	4.95 [33]
K_2ThF_6	X(ThF_4) = 0.33	0.6579	0.6579	0.3824	$\alpha = \beta = 90, \gamma = 120$	$P\bar{6}2$ m	4.92 ± 0.01	
K_2ThF_6	X(ThF_4) = 0.418	0.6576	0.6576	0.3825	$\alpha = \beta = 90, \gamma = 120$	$P\bar{6}2$ m	4.92 ± 0.01	
$K_7Th_6F_{31}$	X(ThF_4) = 0.418	1.5346	1.5346	1.0511	$\alpha = \beta = 90, \gamma = 120$	$R\bar{3}h$	5.24 ± 0.01	5.31 [36]
KTh_2F_9	X(ThF_4) = 0.857	0.8843	1.1602	0.7185	$\alpha = \beta = \gamma = 90$	Pnma	6.07 ± 0.3	6.08 [33]
KTh_6F_{25}	X(ThF_4) = 0.857	0.8326	0.8326	1.6828	$\alpha = \beta = 90, \gamma = 120$	$P6_3mmc$	6.26 ± 0.01	6.29 [33]

[a] Standard uncertainties u are u(X(ThF_4)) = 0.005.
[b] Standard uncertainties u are $u(a)$ = 0.0004 nm.
[c] The reported uncertainties correspond to the standard uncertainty.

Table A.3
Experimental heat capacity data[a] for K_2ThF_6 measured at p = 1.25 mPa[b] and magnetic field B = 0T.

T/K	$C_{p,m}/(J{\cdot}K^{-1}\cdot mol^{-1})$	T/K	$C_{p,m}/(J{\cdot}K^{-1}\cdot mol^{-1})$	T/K	$C_{p,m}/(J{\cdot}K^{-1}\cdot mol^{-1})$
297.03	189.74	183.74	170.36	70.25	77.18
295.03	190.82	181.72	169.64	68.21	74.56
293.01	191.01	179.69	168.78	66.18	71.68
290.97	190.53	177.67	168.05	64.15	68.82
288.95	189.59	175.63	167.14	62.11	65.97
286.92	189.03	173.61	166.28	60.08	63.16
284.90	188.68	171.58	165.22	57.90	60.26
282.88	188.35	169.55	164.41	55.74	57.49
280.85	188.25	167.52	163.57	53.74	54.52
278.84	188.17	165.49	162.54	51.71	51.50
276.82	188.45	163.47	161.54	49.68	48.40
274.80	188.42	161.44	160.50	47.66	45.40
272.79	188.14	159.40	159.38	45.63	42.40
270.75	188.11	157.38	158.39	45.72	42.29
268.73	188.43	155.35	157.24	45.37	41.90
266.72	188.03	153.32	156.14	45.06	41.43
264.70	187.97	151.29	155.07	44.70	40.96
262.68	187.89	149.26	153.99	44.37	40.49
260.66	187.52	147.22	152.74	44.03	39.90
258.64	187.11	145.19	151.37	43.72	39.39
256.61	186.78	143.16	150.03	43.35	38.94
254.58	186.90	141.33	148.26	43.02	38.45
252.56	186.88	139.24	146.86	42.69	37.97
250.55	186.43	137.27	145.46	42.35	37.39
248.52	186.30	135.19	144.28	42.01	36.90
246.49	185.92	133.16	143.36	41.67	36.43
244.46	185.84	131.13	142.04	41.34	35.96
242.43	185.62	129.10	140.29	41.00	35.48
240.41	185.24	127.07	138.50	40.66	35.03
238.38	185.11	125.04	136.69	40.33	34.46
236.35	184.82	123.01	134.92	39.99	33.99
234.32	184.36	120.99	133.24	39.66	33.52
232.30	184.07	118.96	131.32	39.32	33.04
230.27	183.51	116.93	129.37	38.98	32.58
228.25	183.28	114.89	127.37	38.65	32.10
226.23	182.86	112.86	125.17	38.33	31.52
224.21	182.30	110.83	122.95	37.99	31.06
222.19	181.75	108.80	120.81	37.64	30.58
220.16	181.32	106.78	118.68	37.30	30.15
218.14	180.88	104.75	116.36	36.96	29.68
216.12	180.59	102.72	114.16	36.53	29.14
214.09	180.23	100.70	111.71	36.22	28.79
212.06	179.77	98.67	109.43	35.87	28.22
210.04	179.20	96.64	107.12	35.61	27.78
208.02	178.71	94.60	104.33	35.18	27.31
206.00	178.30	92.58	102.10	34.85	26.87
203.98	177.51	90.55	99.94	34.54	26.44
201.96	177.17	88.51	97.50	34.28	25.95
199.94	176.33	86.48	95.04	33.83	25.41
197.92	175.67	84.45	92.73	33.59	24.97
195.89	175.08	82.42	90.57	33.14	24.50
193.87	174.41	80.38	88.56	32.93	23.97
191.84	173.67	78.35	86.30	32.58	23.40
189.81	172.75	76.32	83.97	32.21	22.85
187.79	171.86	74.29	81.66	31.89	22.44
185.77	171.21	72.26	79.47	31.55	22.00
31.21	21.57	12.23	2.482	6.072	0.3053
30.87	21.14	11.89	2.300	5.989	0.2924
30.53	20.61	11.55	2.128	5.904	0.2803
30.20	20.18	11.21	1.961	5.820	0.2681
29.86	19.76	10.87	1.773	5.735	0.2568
29.52	19.35	10.53	1.620	5.651	0.2462
29.18	18.92	10.19	1.478	5.561	0.2339
28.84	18.42	10.18	1.472	5.478	0.2236
28.50	18.00	10.10	1.443	5.393	0.2136
28.17	17.61	10.02	1.408	5.309	0.2044
27.82	17.18	9.936	1.378	5.224	0.1948
27.49	16.77	9.852	1.343	5.139	0.1857
27.15	16.38	9.767	1.312	5.055	0.1773
26.82	15.90	9.683	1.279	4.972	0.1685
26.47	15.51	9.598	1.248	4.887	0.1601
26.14	15.11	9.515	1.215	4.801	0.1523
25.80	14.73	9.431	1.185	4.717	0.1447

(*continued on next page*)

Table A.3 (*continued*)

T/K	$C_{p,m}/(J \cdot K^{-1} \cdot mol^{-1})$	T/K	$C_{p,m}/(J \cdot K^{-1} \cdot mol^{-1})$	T/K	$C_{p,m}/(J \cdot K^{-1} \cdot mol^{-1})$
25.46	14.36	9.349	1.155	4.632	0.1371
25.12	14.01	9.264	1.124	4.548	0.1303
24.78	13.63	9.179	1.096	4.463	0.1235
24.44	13.17	9.096	1.038	4.379	0.1168
24.10	12.79	9.006	1.008	4.294	0.1104
23.75	12.42	8.924	0.9823	4.209	0.1046
23.42	12.06	8.839	0.9555	4.124	0.0986
23.07	11.72	8.757	0.9300	4.041	0.0928
22.73	11.37	8.672	0.9047	3.957	0.0874
22.39	10.94	8.591	0.8792	3.872	0.0823
22.05	10.58	8.505	0.8532	3.787	0.0773
21.71	10.23	8.422	0.8289	3.702	0.0725
21.37	9.891	8.338	0.8047	3.617	0.0681
21.05	9.566	8.254	0.7814	3.534	0.0641
20.69	9.165	8.170	0.7581	3.450	0.0603
20.37	8.854	8.085	0.7353	3.366	0.0565
20.01	8.534	8.002	0.7129	3.276	0.0529
19.70	8.238	7.918	0.6905	3.190	0.0492
19.34	7.909	7.834	0.6685	3.104	0.0459
19.02	7.563	7.749	0.6464	3.018	0.0429
18.66	7.245	7.666	0.6248	2.933	0.0399
18.33	6.959	7.582	0.6041	2.848	0.0373
18.00	6.696	7.497	0.5835	2.764	0.0348
17.65	6.396	7.413	0.5636	2.679	0.0327
17.31	6.116	7.330	0.5441	2.594	0.0304
16.98	5.786	7.244	0.5247	2.509	0.0282
16.64	5.525	7.161	0.5061	2.423	0.0259
16.29	5.264	7.097	0.4924	2.338	0.0242
15.96	5.007	7.002	0.4725	2.253	0.0225
15.62	4.754	6.917	0.4551	2.167	0.0207
15.28	4.508	6.833	0.4382	2.082	0.0190
14.94	4.219	6.749	0.4215	1.999	0.0175
14.60	3.986	6.666	0.4052	1.915	0.0162
14.26	3.760	6.581	0.3895	1.830	0.0149
13.93	3.537	6.497	0.3753		
13.59	3.323	6.413	0.3614		
13.25	3.113	6.329	0.3469		
12.92	2.867	6.242	0.3317		
12.57	2.671	6.156	0.3183		

[a]The standard uncertainties u on the temperature are:
$u(T)$ = 0.01 K for 1.9 < T/K < 20, $u(T)$ = 0.02 K for 20 < T/K < 100,
$u(T)$ = 0.05 K for 100 < T/K < 300.
The relative standard uncertainties on the values of the heat capacities are determined to be $u_r(C_{p,m})$ = 0.03 for T/K < 15,
$u_r(C_{p,m})$ = 0.02 for 15 < T/K < 70, $u_r(C_{p,m})$ = 0.04 for 70 < T/K < 120, $u_r(C_{p,m})$ = 0.01 for 120 < T < 270 K,
and $u_r(C_{p,m})$ = 0.02 for T > 270 K.
[b]The standard uncertainty on the pressure is u(p) = 0.01 mPa.

Using carefully selected data reported in the literature (Table A.1, [14], [49], [50]), the Gibbs energy of formation of $KNaThF_6$ is derived as:

$$\Delta_f G^o_m(KNaThF_6, cr, T) = -3268.52 + 0.5023\ (773 - 848)K \qquad (A.7)$$

Applying the second law of thermodynamics, the enthalpy of formation and entropy of $KNaThF_6$ are deduced at the average measurement temperature (811 K). Having derived $\Delta_f H^o_m(811K)$ and $\Delta_f S^o_m(811K)$, the values at 298.15 K are estimated from the enthalpy increment $\Delta_f H^o_m(T_{ave})$ - $\Delta_f H^o_m(298K)$ calculated with the heat capacity data as given by the Neumann-Kopp rule. Finally, the auxiliary data of the constituent elements of $KNaThF_6$ in Eq. (A.4) can be used again, to obtain $S^o(KNaThF_6, cr, 298K)$. The values so derived are: $\Delta_f H^o_m(KNaThF_6, cr, 298K) = -(3282 \pm 30)$ kJ·mol^{-1}, $S^o_m(KNaThF_6, cr, 298K) = (253.5 \pm 4) J \cdot K^{-1} \cdot$ mol^{-1}.

Appendix C. Lattice parameters of Rietveld and LeBail refinements

Table A.2 lists the lattice parameters of different intermediate phases as refined in this work, as well as a comparison with the literature values and the corresponding space groups.

Appendix D. Experimental heat capacity data and standard thermodynamic functions for K_2ThF_6

The experimental heat capacity data points measured for the phase K_2ThF_6 are listed in Tables A.3 and A.4.

Appendix E. Representative DSC curves

This section contains representative examples of DSC measurements carried out in this work and how the data were extracted. Fig. A.3 is a DSC heating ramp with two event corresponding to eutectic and liquidus temperatures. The intersection between the baseline and the line tangent to the first inflection point of a given event is the onset temperature, T_{onset}, and the temperature assigned to all events except for the liquidus of mixtures. The intersection between the baseline and the line tangent to the second inflection point of a given event is the offset temperature, T_{offset}. In this work, the minimum of the peak, T_{min}, was chosen as the liquidus temperature except for congruent melting. Nevertheless, onset temperatures are also drawn in Fig. 11 as (▽, red) for the liquidus events to illustrate this choice as a likely source of disagreement with previous authors.

Table A.4
Standard thermodynamic functions for K_2ThF_6 at pressure p = 100 kPa. $\phi^o_m(T) = S^o_m(T) - [H^o_m(T) - H^o_m(0)]/T$.[a]

T/K	$C^o_{p,m}(T/K)/$ $(J \cdot K^{-1} \cdot mol^{-1})$	$S^o_m(T/K)/$ $(J \cdot K^{-1} \cdot mol^{-1})$	$H^o_m(T/K) - H^o_m(0)/$ $(kJ \cdot mol^{-1})$	$\phi^o_m(T/K)/$ $(J \cdot K^{-1} \cdot mol^{-1})$
0	0	0	0	–
0.5	2.0800E-03	1.8000E-03	5.04E-07	7.8911E-04
1	5.0000E-03	4.0700E-03	2.23E-06	1.8400E-03
2	0.01681	0.01077	1.31E-05	4.2100E-03
3	0.04276	0.02210	4.29E-05	7.8000E-03
4	0.09114	0.04062	1.10E-04	0.01315
5	0.17144	0.06916	2.41E-04	0.02093
6	0.29413	0.11081	4.74E-04	0.03182
7	0.47013	0.16890	8.56E-04	0.04661
8	0.70965	0.24684	0.00145	0.06609
9	1.0203	0.34787	0.00231	0.09110
10	1.4047	0.47479	0.00352	0.12245
11	1.8475	0.62900	0.00515	0.16086
12	2.3628	0.81143	0.00725	0.20687
13	2.9447	1.0231	0.00991	0.26095
14	3.5882	1.2645	0.01317	0.32348
15	4.2883	1.5356	0.01711	0.39476
16	5.0402	1.8361	0.02178	0.47500
17	5.8403	2.1654	0.02722	0.56433
18	6.6861	2.5229	0.03348	0.66282
19	7.5759	2.9080	0.04061	0.77049
20	8.5088	3.3200	0.04865	0.88733
25	13.800	5.7679	0.10402	1.6073
30	20.023	8.8216	0.18825	2.5465
35	26.881	12.417	0.30532	3.6933
40	34.064	16.473	0.45761	5.0325
45	41.364	20.906	0.64615	6.5466
50	48.679	25.642	0.87127	8.2168
55	55.963	30.624	1.13289	10.026
60	63.183	35.803	1.43079	11.957
65	70.307	41.142	1.76456	13.995
70	77.295	46.609	2.13363	16.129
75	84.106	52.175	2.53721	18.346
80	90.703	57.815	2.97432	20.636
85	97.054	63.506	3.44382	22.990
90	103.13	69.227	3.9444	25.400
95	108.92	74.959	4.47466	27.858
100	114.42	80.687	5.03313	30.356
110	124.51	92.075	6.22872	35.450
120	133.44	103.30	7.51937	40.638
130	141.30	114.30	8.89389	45.883
140	148.19	125.03	10.34208	51.154
150	154.23	135.46	11.85485	56.429
160	159.53	145.59	13.42423	61.686
170	164.18	155.40	15.04329	66.912
180	168.28	164.90	16.70603	72.093
190	171.89	174.10	18.40726	77.222
200	175.10	183.00	20.14253	82.289
210	177.94	191.61	21.90797	87.291
220	180.47	199.95	23.70024	92.224
230	182.73	208.03	25.51644	97.084
240	184.76	215.85	27.35407	101.87
250	186.58	223.43	29.21093	106.58
260	188.23	230.78	31.0851	111.22
270	189.71	237.91	32.97491	115.78
273.15	190.15	240.11	33.57319	117.20
280	191.06	244.83	34.87887	120.26
290	192.29	251.56	36.79569	124.68
298.15	193.20	256.90	38.3666	128.22
300	193.40	258.10	38.72421	129.02

[a]The relative combined standard uncertainties in the values of the fitted heat capacities are determined from the experimental and fitted uncertainties to be $u_r(C_{p,m}) = 0.031$ for T/K < 15, $u_r(C_{p,m}) = 0.021$ for 15 < T/K < 70, $u_r(C_{p,m}) = 0.041$ for 70 < T/K < 120, $u_r(C_{p,m}) = 0.011$ for 120 < T < 270 K, and $u_r\left(C^o_{p,m}\right) = 0.021$ for 270 < T/K.

Fig. A.4 overlays the heating curve of ThF_4 when it is being melted for the first time with the curve of the same ThF_4 sample as it undergoes a second heating cycle, showing that the heat capacity remains the same before and after melting.

Finally, Fig. A.5 is a representative example of a measurement of the mixing enthalpy. The gray area is the mixing event. Note that the curve does not have the pseudo-gaussian shape of the other events in Figs. A.3,A.4, or A.5, but a slightly more complex shape which arises from the endothermic contribution of the melting of KF and ThF_4 and the simultaneous exothermic mixing. Still, as the shading indicates, the total area of the mixing event is measured the same way as for all the other events: as the area constrained by the baseline and the curve which departs from it. Since the areas have opposite signs, they partially cancel each other out, and this is

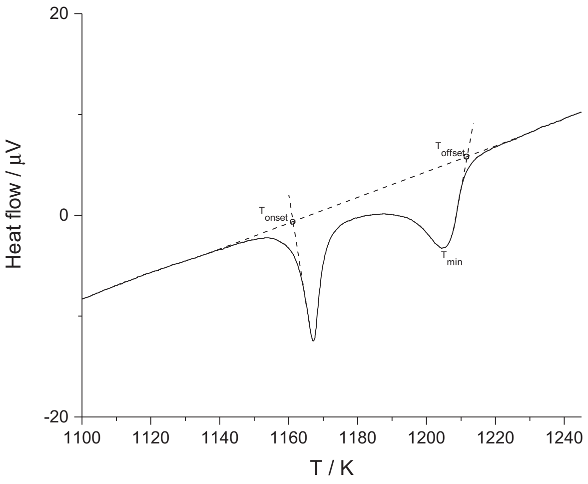

Fig. A.3. Representative example of a DSC heating ramp indicating how T_{onset} and T_{offset} were determined. T_{min} was chosen as the liquidus temperature.

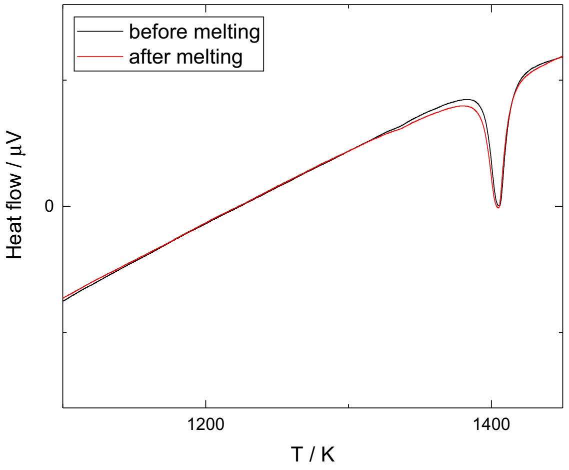

Fig. A.4. DSC heating curve of pure ThF_4 the first time being melted (black, first heating cycle) compared to the second time (red, second heating cycle), showing the heat capacity does not change between cycles. (For interpretation of the references to colour in this figure legend, the reader is referred to the web version of this article.)

taken into account. The second thermal event corresponds to the melting of the silver reference, after the mixing event has concluded, such that they are both well resolved. The fusion of silver is endothermic, yet appears as exothermic because the silver sits in the reference crucible. The superimposed red DSC curve corresponds to a heating ramp of pure ThF_4. Crucially, after the fusion of silver in the mixing enthalpy heating cycle there is no fusion event at the melting temperature of ThF_4; this is an indication of complete mixing. Data from mixing enthalpy measurements were only deduced for those runs which showed complete mixing.

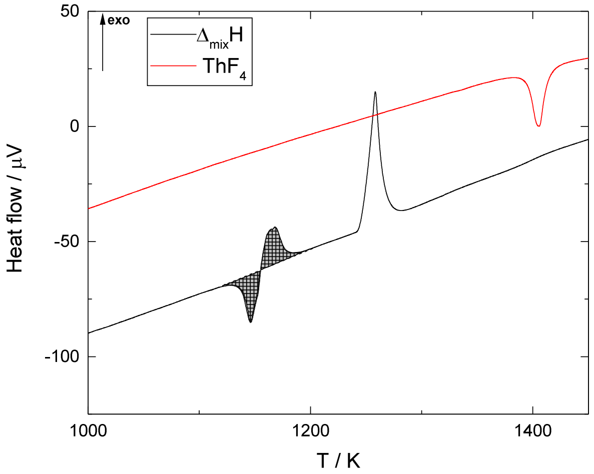

Fig. A.5. Representative example of a mixing enthalpy measurement. Shaded area: [Melting of KF + melting of ThF_4 + mixing of KF with ThF_4]. Second event: melting of the silver reference. Red curve: heating cycle of pure ThF_4 compared against the mixing experiment. (For interpretation of the references to colour in this figure legend, the reader is referred to the web version of this article.)

For every run, a sensitivity could be assigned based on the heat measured on the silver reference, as mentioned in Section 2.5. The total heat measured during the event at the melting temperature of KF, $\Delta_{meas}H^o(T_{fus,KF})$, is given by:

$$\Delta_{meas}H^o(T_{fus,KF}) = S_{salt/Ag} \cdot \frac{Q_{meas}}{S_{Ag,i}} \tag{A.8}$$

where Q_{meas} is the heat measured per mole of sample during the mixing experiment, i.e. the gray area in Fig. A.5, $S_{salt/Ag}$ is the sensitivity coefficient determined during the calibration process, and $S_{Ag,i}$ is the sensitivity of silver during measurement *i*.

Finally, the molar enthalpy of mixing can be derived based on Eq. 1.

Appendix F. Excess Gibbs energy parameters of the consitutent binary liquid solutions

The excess Gibbs energy parameters of the binary solutions needed to calculate the ternary systems were taken from existing assessments and are listed below for completeness.

Table A.5
Extended mixing enthalpy of the $(1-x)$KF(l) + xThF$_4$(l) system determined in this work at T = 1131 ± 10 K and $(0.10 \pm 0.01)^d$ MPa. KF melts at the measurement temperature, while ThF_4 is solid, although the initial state is taken to be a hypothetical liquid. The final state was an undercooled liquid mixture. The scanning temperature range was from (303 ± 10) K to (1373 ± 10) K.

$X(ThF_4)^a$	$\Delta_{mix}H^o_m$ ^{b}/kJ·mol^{-1}	m (KF)/mg^c	m (ThF_4)/mg^c	mass Ag_{ref}/mg^c	$\Delta_{meas}H^o(T_{fus,KF})$ ^{b}/kJ·mol^{-1}
0.109	−15.0 ± 1.4	29.2	18.9	62.0	13.8 ± 1.4
0.200	−29.5 ± 1.8	23.6	31.3	61.9	0.1 ± 1.8
0.305	−30.3 ± 0.2	21.9	50.9	61.80	1.4 ± 0.2
0.338	−30.8 ± 1.0	14.9	40.4	129.0	1.3 ± 1.0
0.401	−31.7 ± 0.7	57.9	16.3	61.8	0.5 ± 0.7
0.504	−32.9 ± 3.0	39.3	7.3	61.7	1.7±3.0

[d] The quoted uncertainty corresponds to the standard uncertainty.
[a] Standard uncertainties u are u(X(ThF_4)) = 0.005.
[b] The error is based on the standard uncertainty determined during calibration.
[c] Standard uncertainties u are u(m) = 0.1 mg.

$$\Delta g_{LiK/FF} = -7615 + 4.861 \cdot T - 0.001674 \cdot T^2 + (-958 + 1.255 \cdot T)\chi_{LiK/FF} + (-690 + 1.966 \cdot T)\chi_{KLi/FF} J \cdot mol^{-1} \quad (A.9)$$

(JRCSMSD thermodynamic database on halide salts, JRC-Karlsruhe.)

$$\Delta g_{LiTh/FF} = -10878 + (-6694 + 2.929 \cdot T)\chi_{LiTh/FF} + (-20920 + 19.46 \cdot T)\chi_{ThLi/FF} J \cdot mol^{-1} \quad (A.10)$$

(JRCSMSD thermodynamic database on halide salts, JRC-Karlsruhe.)

$$\Delta g_{NaK/FF} = -118 + 0.847 \cdot TJ \cdot mol^{-1} \quad (A.11)$$

[51]

$$\Delta g_{NaTh/FF} = -26784 + (10046 - 12.56 \cdot T)\chi_{NaTh/FF} + (-30106 + 16.74 \cdot T)\chi_{ThNa/FF} J \cdot mol^{-1} \quad (A.12)$$

[24]

References

[1] GIF, Annual report 2013, Generation IV International Forum (Tech. Rep.). www.gen-4.org/gif/upload/docs/application/pdf/2014-06/gif_2013_annual_report-final.pdf (2013).
[2] GIF, Technology Roadmap Update for Generation IV Nuclear Energy Systems (Tech. Rep.).www.gen-4.org/gif/upload/docs/application/pdf/2014-03/gif-tru2014.pdf (2014).
[3] E.S. Bettis, R.W. Schroeder, G.A. Cristy, H.W. Savage, R.G. Affel, L.F. Hemphill, Nucl. Sci. Eng. 2 (6) (1957) 804–825.
[4] P.N. Haubenreich, J.R. Engel, Nucl. Technol. 8 (2) (1970) 118–136.
[5] C.Renault, M. Hron, R.J.M. Konings, D.-E. Holcomb, in: GIF Symposium, Paris (France), 9–10 September 2009, pp. 191–200.
[6] R.E. Thoma, H.A. Friedman, R.A. Penneman, J. Am. Chem. Soc. 88 (9) (1966) 2046–2047.
[7] R.E. Thoma, H. Insley, B.S. Landau, H.A. Friedman, W.R. Grimes, J. Am. Ceram. Soc. 41 (12) (1958) 538–544.
[8] V.S. Emelyanov, A.I. Evstyukhin, J. Nucl. Energy (1954) 5 (1) (1957) 108–114.
[9] W.J. Asker, E.R. Segnit, A.W. Wylie, J. Chem. Soc. (Resumed) (1952) 4470–4479.
[10] P. Souček, O. Beneš, B. Claux, E. Capelli, M. Ougier, V. Tyrpekl, J.F. Vigier, R.J.M. Konings, J. Fluorine Chem. 200 (2017) 33–40.
[11] J. Rodriguez-Carvajal, Phys. B 192 (1993) 55–69.
[12] O. Beneš, R.J.M. Konings, S. Wurzer, M. Sierig, A. Dockendorf, Thermochim. Acta 509 (1–2) (2010) 62–66.
[13] William J. Boettinger, Ursula R. Kattner, Kil-Won Moon, John H. Perepezko, in: J.-C. Zhao (Ed.), Methods for Phase Diagram Determination, Elsevier Science Ltd, Oxford, 2007, pp. 151 – 221.
[14] M.W. Chase, NIST-JANAF Thermochemical Tables (Journal of Physical and Chemical Reference Data Monograph No. 9) (1998).
[15] R.J.M Konings, J.P.M Vander Meer, E.Walle. Tech. Rep., ITU-TN 2005/25, Technical report, 2005.
[16] E. Capelli, O. Beneš, M. Beilmann, R.J.M. Konings, J. Chem. Thermodyn. 58 (2013) 110–116.
[17] I. Ansara, B. Sundman, Scientific Group Thermodata Europe, Computer Handling and Determination of Data, North Holland, Amsterdam, 1986.
[18] J.C. Lashley, M.F. Hundley, A. Migliori, J.L. Sarrao, P.G. Pagliuso, T.W. Darling, M. Jaime, J.C. Cooley, W.L. Hults, L. Morales, et al., Cryogenics 43 (6) (2003) 369–378.
[19] P. Javorsk, F. Wastin, E. Colineau, J. Rebizant, P. Boulet, G. Stewart, J. Nucl. Mater. 344 (1-3) (2005) 50–55.
[20] A.L. Smith, M.-C. Pignié, Lvan Eijck, J.-C. Griveau, Eric Colineau, R.J.M. Konings, J. Chem. Thermodyn. 120 (2018) 205–216.
[21] H.L. Lukas, S.G. Fries, B. Sundman, Computational Thermodynamics. The Calphad Method, Cambridge University Press, 2007.
[22] C.W. Bale, E. Bélisle, P. Chartrand, S.A. Decterov, G. Eriksson, A.E. Gheribi, K. Hack, I.-H. Jung, Y.-B. Kang, J. Melançon, A.D. Pelton, S. Petersen, C. Robelin, J. Sangster, P. Spencer, M.-A. Van Ende, Calphad 54 (2016) 35–53.
[23] J. Leitner, P. Voňka, D. Sedmidubský, P. Svoboda, Thermochim. Acta 497 (1–2) (2010) 7–13.
[24] E. Capelli, O. Beneš, R.J.M. Konings, J. Nucl. Mater. 449 (1) (2014) 111–121.
[25] S. Mukherjee, S. Dash, J. Radioanal. Nucl. Chem. 313 (3) (2017) 481–486.
[26] O. Beneš, M. Beilmann, R.J.M. Konings, J. Nucl. Mater. 405 (2) (2010) 186–198.
[27] O. Beneš, R.J.M. Konings, Calphad 32 (1) (2008) 121–128.
[28] O. Beneš, M. Beilmann, R.J.M. Konings, J. Nucl. Mater. 405 (2) (2010) 186–198.
[29] A.D. Pelton, S.A. Degterov, G. Eriksson, C. Robelin, Y. Dessureault, Metall. Mater. Trans. B 31 (4) (2000) 651–659.
[30] A.D. Pelton, Calphad 25 (2) (2001) 319–328.
[31] E.P. Dergunov, A.G. Bergman, Doklady Akademii Nauk SSSR 60 (3) (1948) 391–394.
[32] R.R. Ryan, R.A. Penneman, Acta Crystallogr. Section B 27 (4) (1971) 829–833.
[33] W.H. Zachariasen, J. Am. Chem. Soc. 70 (6) (1948) 2147–2151.
[34] R.E. Thoma, Oak Ridge National Lab., Tenn., Technical report, 1958.
[35] G. Brunton, Acta Crystallogr. Section B 27 (11) (1971) 2290–2292.
[36] A. Grzechnik, C.C. Underwood, J.W. Kolis, K. Friese, J. Fluorine Chem. 150 (2013) 8–13.
[37] J. Majzlan, A. Navrotsky, B.F. Woodfield, B.E. Lang, J. Boerio-Goates, R.A. Fisher, J. Low Temp. Phys. 130 (1–2) (2003) 69–76.
[38] B.F. Woodfield, J. Boerio-Goates, J.L. Shapiro, R.L. Putnam, A. Navrotsky, J. Chem. Thermodyn. 31 (2) (1999) 245–253.
[39] B.F. Woodfield, Jennifer L. Shapiro, R. Stevens, J. Boerio-Goates, R.L. Putnam, K. B. Helean, A. Navrotsky, J. Chem. Thermodyn. 31 (12) (1999) 1573–1583.
[40] S.J. Smith, R. Stevens, S. Liu, G. Li, A. Navrotsky, J. Boerio-Goates, B.F. Woodfield, Am. Mineral. 94 (2–3) (2009) 236–243.
[41] E.S.R. Gopal, Specific heats at low temperatures (international cryogenics monograph series), 1966.
[42] N. Vozárová, A.L. Smith, J.Y. Colle, P.E. Raison, D. Bouëxière, R.J.M. Konings, O. Beneš, J. Chem. Thermodyn. 114 (2017) 71–82.
[43] O. Pauvert, M. Salanne, D. Zanghi, C. Simon, S. Reguer, D. Thiaudire, Y. Okamoto, H. Matsuura, C. Bessada, J. Phys. Chem. B 115 (29) (2011) 9160–9167, PMID:21675783.
[44] M. Salanne, C. Simon, P. Turq, R.J. Heaton, P.A. Madden, J. Phys. Chem. B 110 (23) (2006) 11461–11467.
[45] M. Salanne, C. Simon, P. Turq, P.A. Madden, J. Phys. Chem. B 111 (18) (2007) 4678–4684.
[46] E. Rabani, J.D. Gezelter, B.J. Berne, J. Chem. Phys. 107 (17) (1997) 6867–6876.
[47] S.N. Flengas, A.S. Kucharski, Can. J. Chem. 49 (24) (1971) 3971–3985.
[48] C. Bessada, A. Rakhmatullin, D. Rollet, A.L. Zanghi, J. Nucl. Mater. 360 (1) (2007) 43–48.
[49] H. Gamsjäger, J. Bugajski, T. Gajda, R.J. Lemire, W. Preis, Chemical Thermodynamics of Nickel, OECD Nuclear Energy Agency, Data Bank, Issy-les-Moulineaux (France), 2005.
[50] M.H. Rand, F.J. Mompean, J. Perrone, M. Illemassène, Chemical Thermodynamics of Thorium. Chemical Thermodynamics, OECD Pub., 2008.
[51] O. Beneš, Thermodynamics of molten salts for nuclear applications (PhD thesis, Ph. D. Dissertation), Institute of Chemical Technology, Prague, 2008.

JCT 2019-349